

See discussions, stats, and author profiles for this publication at: <https://www.researchgate.net/publication/348790466>

# 3GPP TR 38.901 Channel Model

Chapter · January 2021

DOI: 10.1002/9781119471509.w5gref048

CITATIONS

50

READS

9,929

6 authors, including:



**Qiuming Zhu**

Nanjing University of Aeronautics & Astronautics

199 PUBLICATIONS 1,441 CITATIONS

SEE PROFILE



**Cheng-Xiang Wang**

Heriot-Watt University

456 PUBLICATIONS 16,383 CITATIONS

SEE PROFILE



**Boyu Hua**

Nanjing University of Aeronautics & Astronautics

46 PUBLICATIONS 371 CITATIONS

SEE PROFILE



**Mao Kai**

Nanjing University of Aeronautics & Astronautics

70 PUBLICATIONS 501 CITATIONS

SEE PROFILE

# 3GPP TR 38.901 Channel Model

Qiuming Zhu<sup>1,\*</sup>, Cheng-Xiang Wang<sup>2,3,\*</sup>, Boyu Hua<sup>1</sup>, Kai Mao<sup>1</sup>, Shan Jiang<sup>1</sup>  
and Mengtian Yao<sup>1</sup>

<sup>1</sup> The Key Laboratory of Dynamic Cognitive System of Electromagnetic Spectrum Space,  
College of Electronic and Information Engineering,  
Nanjing University of Aeronautics and Astronautics, Nanjing 211106, China

<sup>2</sup> National Mobile Communications Research Laboratory, School of Information Science and Engineering,  
Southeast University, Nanjing 210096, China

<sup>3</sup> Purple Mountain Laboratories, Nanjing 211111, China

\* Corresponding author : chxwang@seu.edu.cn, zhuqiuming@nuaa.edu.cn

Word Count: about 8110

## Abstract

The 3rd Generation Partnership Project (3GPP) recommends an accurate and compatible stochastic channel model for 0–100 GHz frequency band, which is useful to design, optimize, and evaluate the fifth generation (5G) systems. This standardized model can be acquired by generating the large-scale fading model and small-scale fading model. This chapter firstly reviews the main existing channel models suitable for millimeter-wave (mmWave) frequency band as well as the typical channel modeling methods, i.e., the deterministic and stochastic models. Secondly, the generation procedure of stochastic channel model in the 3GPP standard (TR 38.901) is illustrated in details. The large-scale fading part and small-scale fading part are also simulated to demonstrate the effect of channel parameters on the channel characteristic. Finally, as an alternative model in the 3GPP standard, the map-based hybrid channel model is demonstrated and analyzed. When the digital map and material parameters of obstacles are known, this model can predict the channel characteristic accurately by using the ray tracing (RT) method.

## Index Terms

3GPP, mmWave, 5G channel model, large-scale fading, small-scale fading, RT

## I. INTRODUCTION

The fifth generation (5G) systems allow to access and share information in a diverse variety of scenarios, e.g., indoor, urban, suburban, and rural area, with extremely low latency and high data rate. The new system achieves 1000 times the system capacity, 100 times the data rate, 5–15 times the spectral efficiency, 10 times the connectivity density target, 100 times the cost efficiency with respect to the fourth generation (4G) systems [1]–[3].

The expected goals of 5G system performance drives the need for greater bandwidth. However, the available bandwidth for current sub-6 GHz systems can not satisfy the requirements. One of the most important technologies for 5G systems is millimeter-wave (mmWave) communication. Note that the mmWave channels have some new characteristics as well as high path loss and multi-path sparsity, which are caused by high frequency and high time resolution. Therefore, it is vital to explore accurate and compatible mmWave channel models for designing, optimizing, and evaluating 5G systems [4]–[7].

For the mmWave band, a number of different channel models have been proposed [8]–[27]. These channel models can be classified into two categories, i.e., the deterministic and stochastic models [28], [29]. The deterministic mmWave channel models are supposed to have constant channel parameters, which means the statistical properties of each simulation are fixed. In addition, the channel parameters can be obtained by the ray-tracing (RT) method or measurement approaches [30]–[33]. For example, the mmWave channel parameters under urban scenarios were analyzed by RT simulations in [8], [9]. The RT-based deterministic mmWave channel models of suburban, rural, mountain, marine, and campus scenarios can be addressed in [10]–[14]. It is noteworthy that the RT-based channel models usually need a specific digital map with high accuracy. To precisely take the effect of obstacles and environment details into account, laser-scanning techniques were used to describe the exact scenario as a set of points, namely a point cloud [15]. The point cloud method based on measured results is an alternative prediction approach to characterize the propagation channel parameters with higher precision [16]. On the other hand, the stochastic mmWave channel models are supposed to have at least one random channel parameter which is described by the distribution extracting from analytical or

measured results. For example, based on the measurement results, the Saleh-Valenzuela (SV) model clustered the multi-path components in the delay and angle domains and generated the random mmWave channel parameters [17], [18]. The propagation graph channel model utilized vertices to represent the transmitters (Tx), receivers (Rx), and scatterers, then utilized edges with random probability values to represent the propagation conditions between the vertices [19]. The geometry based stochastic model (GBSM) is the most widespread stochastic channel model, which calculates the channel parameters according to the randomly distributed scatterers [20]–[26]. The authors in [27] used the geometry-based approach to analyze the mmWave channel characteristics. Note that RT-based channel models usually need the specific map and complex computation. A hybrid method combining the RT method and GBSM, namely map-based hybrid channel model, is developed in the 3rd Generation Partnership Project (3GPP) standardized model which will be demonstrated in details in this chapter.

With the development of mmWave channel research, several channel models have been standardized or widely accepted, i.e., 3GPP channel model [34], QuaDRiGa channel model [35]–[37], IMT-2020 channel model [38], mmMAGIC channel model [39], IEEE 802.11ay [40] channel model, METIS channel model [41], MiWEBA channel model [42], [43], 5GCMSIG channel model [44], and COST 2100 channel model [45], [46]. All of these channel models, except MiWEBA and IEEE 802.11ay, can be categorized as GBSMs and originate from the 3GPP-SCM model [47] or the WINNER II [48] model. Note that the grid-based GBSM was first proposed by METIS and then adopted by 5GCMSIG and mmMAGIC. It can provide a smooth time evolution and spatially consistent simulations. The map-based hybrid channel model in the 3GPP standard combined the deterministic and stochastic channel modeling methods. Channel parameters were divided into two parts, i.e., deterministic parameters obtained from the RT method and random parameters obtained from measurement data. This idea can achieve a balance between the complexity and accuracy [49].

The 3GPP consists of seven telecommunications standard development organizations, i.e., ARIB, ATIS, CCSA, ETSI, TSDSI, TTA, and TTC. The project aims to provide a stable environment for producing the reports and specifications to define the related technologies [34], [50]. Note that the reports and specifications involve all the technology

description for a complete mobile communication system, i.e., radio access, core network, and service capabilities. As shown in Fig. 1, the 3GPP channel model (3GPP TR 38.901) specification is the one that aims to help communication engineers to evaluate the performance of physical layer techniques in the fifth generation (5G) system [51], [52]. The timeline of 3GPP standardization for 5G systems is shown in Fig. 2. The 3GPP TR 38.901 specification is suitable for frequencies from 0.5 GHz to 100 GHz, and also compatible with the earlier specifications, e.g., the three-dimensional spatial channel model (3GPP TR 36.873) and IMT-Advanced (ITU-R M.2135) [53]–[56]. Meanwhile, the standardized channel model can be used for both link and system level simulations under various scenarios such as macrocell (UMa), urban microcell street canyon (UMi-Street Canyon), rural macro (RMa), indoor hotspot office (InH-office), and indoor factory (InF) [57]–[59].

In this chapter, we firstly analyze the stochastic channel model recommended by the 3GPP standard of TR 38.901. The model includes two parts, i.e., the large-scale fading and the small-scale fading. The large-scale fading modeling involves the LOS probability, path loss, and other additional losses, while the small-scale fading part focuses on the effect of multiple-path and movements of terminals on the propagation channel. Then, as an alternative model, the map-based hybrid channel model is demonstrated and analyzed. This model can be used to reproduce the channel characteristic accurately, when the digital map and material parameters of obstacles are known. Finally, conclusions are drawn.

## II. STOCHASTIC CHANNEL MODEL

### A. Large-scale fading model

#### 1) Framework:

When the additional modeling components, i.e., spatial consistency, large bandwidth or arrays, and blockage are not included, the 3GPP stochastic channel model can be obtained by the procedure containing the large-scale fading and the small-scale fading. For the large-scale fading model, users firstly set an interesting scenario, i.e., UMa,

UMi-Street canyon, RMa, InH-office, and InF, as well as the number of antennas and velocity parameters, then obtain the channel parameters by the procedure shown in Fig. 3. In the figure, each user terminal (UT) has an indoor or outdoor state and all the links with the same UT share one state. The calculation methods of some specific and important parameters are illustrated in the following.

### 2) *LOS probability:*

In order to character the propagation condition, the line of sight (LOS) probability for specific scenarios is introduced to describe the chance of LOS component existence [60]–[63]. The 3GPP channel model defines some LOS probability models in which the antenna heights are 3 m for indoor, 10 m for UMi, and 25 m for UMa, as shown in Table I. Note that the InF scenario can be further divided into the indoor factory with sparse clutters and low base station height (InF-SL), the indoor factory with dense clutters and low base station height (InF-DL), the indoor factory with sparse clutters and high base station height (InF-SH), the indoor factory with dense clutters and high base station height (InF-DH), and the indoor factory with high transmitter (Tx) and high receiver (Rx) (InF-HH). Fig. 4 shows the parameters when UTs are settled outdoor and indoor, where  $d_{3D-in}$  and  $d_{2D-in}$  describe the locations of indoor UTs in three-dimensional (3D) and two-dimensional (2D) distances, respectively.

Based on the methods in Table I, five LOS probability models with the UT height of 1.5 m under the RMa, UMi-Street canyon, UMa, InH-Office, and InF scenarios are calculated and compared in Fig. 5. It can be seen that different propagation scenarios lead to different LOS probabilities. The InF-HH scenario has the highest probability as 1 because there are no obstacles between the high Tx and high Rx. As an open area, the RMa scenario has the second highest LOS probability. The InF-DL scenario has the lowest LOS probability due to the largest number of obstacles compared to other scenarios.

### 3) *Path loss:*

The path loss is the major component in the large-scale fading model and has a strong relevance to the distance [64]–[68]. When UTs are fixed as shown in Fig. 4, the geometric relationship of distance can be expressed as

$$d_{3D-out} + d_{3D-in} = \sqrt{(d_{2D-out} + d_{2D-in})^2 + (h_{BS} - h_{UT})^2} \quad (1)$$

where the parameters  $d_{3D-in}$  and  $d_{2D-in}$  describe the 3D and 2D indoor distances, respectively.

For the scenarios of interest, the corresponding path loss models provided by the 3GPP channel model are summarized in Table II. In the table, the break point distance can be expressed as  $d_{BP} = 2\pi h_{BS} h_{UT} f_c / c$ , where  $f_c$  is the carrier frequency,  $c$  is the speed of light in the free space,  $h_{BS}$  and  $h_{UT}$  denote the heights of antenna at the BS and UT, respectively. Another break point distance is  $d'_{BP} = 4h'_{BS} h'_{UT} f_c / c$ , where the effective antenna heights  $h'_{BS}$  and  $h'_{UT}$  are calculated as  $h'_{BS} = h_{BS} - h_E$ ,  $h'_{UT} = h_{UT} - h_E$ , where the  $h_E$  is the effective environment height. It should be mentioned that the shadow fading follows the log-normal distribution as shown in Table II. The standard deviation (STD) under different scenarios including the LOS and none line of sight (NLOS) conditions are also given.

Taking the RMa scenario as an example, the LOS and NLOS path loss models are simulated and shown in Fig. 6. In the simulation, the antenna height values are  $h_{BS} = 35$  m,  $h_{UT} = 1.5$  m,  $W = 20$  m, and  $h = 5$  m. It is clearly shown that the path loss in the LOS scenario is smaller than the one of the NLOS scenario. Moreover, the difference of path loss between the LOS and NLOS scenarios is gradually increasing within 1000 meters and then basically unchanged after 1000 meters.

#### 4) Additional loss:

Besides the path loss due to the communication distance, several other additional losses, e.g., the penetration loss and oxygen absorption loss, are also considered in the 3GPP channel model. The penetration loss  $PL_{tw}$  can be expressed as

$$PL_{tw} = PL_{npi} - 10 \log_{10} \sum_{i=1}^N \left( p_i \times 10^{\frac{L_{material\_i}}{-10}} \right) \quad (2)$$

where  $PL_{npi}$  is the external wall loss by non-perpendicular incidence,  $p_i$  is proportion of  $i$ -th materials with  $\sum_{i=1}^N p_i = 1$ , and  $N$  means the total number of materials. In addition,  $L_{material\_i} = a_{material\_i} + b_{material\_i} \cdot f$  denotes the penetration loss caused by material  $i$  and  $f$  in GHz. The typical values of penetration loss are given in Table III.

Two empirical models of path loss through the external wall can be found in Table IV. The corresponding simulation results are given in Fig. 7. It is obviously shown that the gap between high-loss model and low-loss model increases as the carrier frequency increases.

The path loss including outdoor-to-indoor (O2I) building penetration loss can be modeled as

$$PL = PL_b + PL_{tw} + PL_{in} + N(0, \sigma_P^2) \quad (3)$$

where  $PL_b$  is the outdoor path loss,  $PL_{tw}$  denotes the above building penetration loss with the corresponding std  $\sigma_P$ , and  $PL_{in}=0.5d_{2D-in}$  means the indoor path loss due to the depth into the building. For the single sub-6 GHz frequency simulation, a set of parameters can be found in the standardized model as  $PL_{tw}=20$  dB,  $\sigma_P=0$ ,  $PL_{in}=0.5d_{2D-in}$ ,  $0 < d_{2D-in} < 25$  m.

As a special case, the penetration loss of a regular car can be considered as zero. Thus, the path loss including O2I car penetration loss can be calculated as

$$PL = PL_b + N(\mu, \sigma_P^2) \quad (4)$$

where  $\sigma_P = 5$  and  $\mu$  depends on the car. For example, it is recommended that  $\mu = 20$  for the metallized car window. Note that the applicable frequency band of O2I car penetration loss model is at least from 0.6 GHz to 60 GHz.

Oxygen absorption loss is also considered in the 3GPP channel model as another kind of additional loss. The additional loss caused by oxygen absorption can be calculated by

$$OL_n(f_c) = \frac{\alpha(f_c)}{1000} \cdot (d_{3D} + c \cdot \Delta\tau) \quad (5)$$

where  $\alpha(f_c)$  is frequency dependent oxygen loss coefficient as shown in Table V,  $c \cdot \Delta\tau$  denotes the extra travel distance compared with the LOS path and  $\Delta\tau$  is the relative delay.

Note that coefficient for the center frequency not listed in Table V can be calculated by a linear interpolation as shown in Fig. 8. The simulated result shows that oxygen absorption loss occurs while the frequency is in the range of 52 GHz to 68 GHz, and the values are all zero when the frequency is out of that range. Moreover, the oxygen



absorption loss achieves the maximum, i.e., 15 dB/km, when the frequency is 60 GHz.

5) *Shadowing correlation:*

The log-normal distribution is adopted in the 3GPP channel model to describe the shadowing. In the logarithmic scale, it is characterized as around the mean value of path loss with a zero-mean Gaussian distribution. The shadowing is a slow fading process over distance, and thus the adjacent fading states should be distance- or time- correlated. In the 3GPP channel model, the normalized autocorrelation function is modeled by an exponential function as

$$R(\Delta x) = e^{-\frac{|\Delta x|}{d_{\text{cor}}}} \quad (6)$$

where  $d_{\text{cor}}$  denotes the correlation distance and depends on the environment condition. For the case of spatial consistency, the random variables of cluster are also correlated and follow the exponential function regarding to the correlation distance in the two-dimensional horizontal plane.

*B. Small-scale fading model*

1) *Framework:*

The large-scale fading model depicts the LOS probability, path loss, other additional losses, and the shadowing correlation, while the small-scale fading model is defined by the channel impulse response (CIR) and generated with the parameters of cluster and inter-cluster. The procedure to calculate and generate the small-scale parameters and coefficients is illustrated in Fig. 9.

The CIR consists of two parts, i.e., the LOS and NLOS propagation paths, and can be expressed as

$$H_{u,s}(\tau, t) = \sqrt{\frac{1}{K_R(t) + 1}} H_{u,s}^{\text{NLOS}}(\tau, t) + \sqrt{\frac{K_R(t)}{K_R(t) + 1}} H_{u,s}^{\text{LOS}} \delta(\tau - \tau_1) \quad (7)$$

where  $\delta(\tau)$  is the Dirac's delta function and  $K_R$  is the Ricean K-factor,  $u$  and  $s$  represent the Tx antenna element and Rx antenna element, respectively. Furthermore, the NLOS component is modeled by the summation of  $N$  clusters including 2 strongest clusters and

$N-2$  weakest clusters, and can be described as

$$H_{u,s}^{\text{NLOS}}(\tau, t) = \sum_{n=1}^2 \sum_{i=1}^3 \sum_{m \in R_i} H_{u,s,n,m}^{\text{NLOS}}(t) \delta(\tau - \tau_{n,i}) + \sum_{n=3}^N H_{u,s,n}^{\text{NLOS}}(t) \delta(\tau - \tau_n) \quad (8)$$

where  $n$  denotes a cluster,  $m$  denotes a ray within cluster  $n$ ,  $H_{u,s,n}^{\text{NLOS}}(t)$  denotes the channel coefficient of the  $N-2$  weakest clusters and is given by

$$H_{u,s,n}^{\text{NLOS}}(t) = \sqrt{\frac{P_n}{M}} \sum_{m=1}^M \begin{bmatrix} F_{rx,u,\theta}(\theta_{n,m,ZOA}, \phi_{n,m,AOA}) \\ F_{rx,u,\phi}(\theta_{n,m,ZOA}, \phi_{n,m,AOA}) \end{bmatrix}^T \begin{bmatrix} e^{j\Phi_{n,m}^{\theta\theta}} & \sqrt{\kappa_{n,m}^{-1}} e^{j\Phi_{n,m}^{\theta\phi}} \\ \sqrt{\kappa_{n,m}^{-1}} e^{j\Phi_{n,m}^{\phi\theta}} & e^{j\Phi_{n,m}^{\phi\phi}} \end{bmatrix} \begin{bmatrix} F_{tx,s,\theta}(\theta_{n,m,ZOD}, \phi_{n,m,AOD}) \\ F_{tx,s,\phi}(\theta_{n,m,ZOD}, \phi_{n,m,AOD}) \end{bmatrix} e^{\frac{j2\pi(\hat{r}_{rx,n,m}^T \cdot \bar{d}_{rx,u})}{\lambda_0}} e^{\frac{j2\pi(\hat{r}_{tx,n,m}^T \cdot \bar{d}_{tx,s})}{\lambda_0}} e^{j2\pi \frac{\hat{r}_{rx,n,m}^T \cdot \bar{v}}{\lambda_0} t} \quad (9)$$

where  $P_n$  is the cluster power and will be discussed in the following section,  $F_{rx,u,\theta}$  and  $F_{rx,u,\phi}$  are the field patterns of the  $u$ -th receiving antenna element,  $\theta_{ZOA}, \phi_{AOA}$  denote the zenith and azimuth angles of arrival signal, respectively, the scalar  $e^{j\Phi_{n,m}}$  represents the vertically polarized field patterns,  $F_{tx,s,\theta}$  and  $F_{tx,s,\phi}$  are the field patterns of the  $s$ -th transmitting antenna element in the direction of the spherical basis vectors,  $\theta_{ZOD}, \phi_{AOD}$  denote the corresponding zenith and azimuth angles of departure signal, respectively,  $\hat{r}_{tx,n,m}^T$  is the spherical unit vector and  $\bar{d}$  is the location vector of Tx antenna element  $s$  and Rx antenna element  $u$ , respectively. In addition,  $H_{u,s,n,m}^{\text{NLOS}}(t)$  is defined as

$$H_{u,s,n,m}^{\text{NLOS}}(t) = \sqrt{\frac{P_n}{M}} \begin{bmatrix} F_{rx,u,\theta}(\theta_{n,m,ZOA}, \varphi_{n,m,AOA}) \\ F_{rx,u,\phi}(\theta_{n,m,ZOA}, \varphi_{n,m,AOA}) \end{bmatrix}^T \begin{bmatrix} e^{j\Phi_{n,m}^{\theta\theta}} & \sqrt{\kappa_{n,m}^{-1}} e^{j\Phi_{n,m}^{\theta\varphi}} \\ \sqrt{\kappa_{n,m}^{-1}} e^{j\Phi_{n,m}^{\phi\theta}} & e^{j\Phi_{n,m}^{\phi\varphi}} \end{bmatrix} \begin{bmatrix} F_{tx,s,\theta}(\theta_{n,m,ZOD}, \varphi_{n,m,AOD}) \\ F_{tx,s,\phi}(\theta_{n,m,ZOD}, \varphi_{n,m,AOD}) \end{bmatrix} e^{\frac{j2\pi\hat{r}_{rx,n,m}^T \cdot \bar{d}_{rx,u}}{\lambda_0}} e^{\frac{j2\pi\hat{r}_{tx,n,m}^T \cdot \bar{d}_{tx,s}}{\lambda_0}} e^{j2\pi \frac{\hat{r}_{rx,n,m}^T \cdot \bar{v}}{\lambda_0} t} \quad (10)$$

For the LOS case, the channel coefficient can be obtained by

$$H_{u,s,1}^{\text{LOS}}(t) = \begin{bmatrix} F_{rx,u,\theta}(\theta_{\text{LOS},ZOA}, \varphi_{\text{LOS},AOA}) \\ F_{rx,u,\phi}(\theta_{\text{LOS},ZOA}, \varphi_{\text{LOS},AOA}) \end{bmatrix}^T \begin{bmatrix} 1 & 0 \\ 0 & -1 \end{bmatrix} \begin{bmatrix} F_{tx,s,\theta}(\theta_{\text{LOS},ZOD}, \varphi_{\text{LOS},AOD}) \\ F_{tx,s,\phi}(\theta_{\text{LOS},ZOD}, \varphi_{\text{LOS},AOD}) \end{bmatrix} e^{\left(-\frac{j2\pi d_{3D}}{\lambda_0}\right)} e^{\frac{j2\pi\hat{r}_{rx,\text{LOS}}^T \cdot \bar{d}_{rx,u}}{\lambda_0}} e^{\frac{j2\pi\hat{r}_{tx,\text{LOS}}^T \cdot \bar{d}_{tx,s}}{\lambda_0}} e^{\frac{j2\pi\hat{r}_{rx,\text{LOS}}^T \cdot \bar{v}}{\lambda_0} t} \quad (11)$$

2) *Delay and power parameters:*

Different propagation paths result in various delays [69], which can be obtained randomly from the delay distribution in the 3GPP channel model as

$$\tau'_n = -r_\tau DS \ln(X_n) \quad (12)$$

where  $r_\tau$  is the delay distribution proportionality factor,  $X_n$  is a random variable following the uniform distribution over (0,1),  $DS$  follows the logarithmic normal distribution shown in Table VI. Normalize the delays by subtracting the minimum delay and sort in ascending order as

$$\tau_n = \text{sort}(\tau'_n - \min(\tau'_n)). \quad (13)$$

For the LOS condition, the scaled delay is

$$\tau_n^{\text{LOS}} = \tau_n / C_\tau \quad (14)$$

where  $C_\tau$  is Ricean K-factor dependent scaling constant and can be found in Table VI.

Cluster power is calculated by a single slope exponential model with respect to the corresponding delay in the 3GPP channel model [70]. With the exponential delay distribution, the cluster power can be calculated by

$$P'_n = \exp\left(-\tau_n \frac{r_\tau - 1}{r_\tau DS}\right) \cdot 10^{\frac{-Z_n}{10}} \quad (15)$$

where  $Z_n \sim N(0, \zeta^2)$  denotes the cluster shadowing effect and  $\zeta$  denotes the per cluster shadowing STD. Finally, normalize all cluster powers and make the sum of all cluster powers equal to one, i.e.,

$$P_n = \frac{P'_n}{\sum_{n=1}^N P'_n} \quad (16)$$

where  $N$  is the number of clusters.

For the LOS condition, an additional specular component is added to the first cluster, and the cluster powers is normalized as

$$P_n = \frac{1}{K_R + 1} \frac{P'_n}{\sum_{n=1}^N P'_n} + \delta(n-1) P_{1,\text{LOS}} \quad (17)$$

where  $P_{1,\text{LOS}}$  is the power of single LOS ray, and  $K_R$  is the Ricean K-factor defined in

the last subsection.

Based on (12) – (17) and the parameters in Table VI, a series of simulation are carried out to illustrate the generation procedure of delays and powers in the 3GPP channel model. Under the LOS scenario, two simulation results of power delay profile (PDP) are shown in Fig. 10(a) and Fig. 10(b), respectively. By repeating the simulation for 10,000 times, the averaged PDP is given in Fig. 11. As we can see that  $P_n$  exclude the LOS part follows a single slope exponential model. Since the cumulative distribution function (CDF) of delay is over 95% when the delay equals 2500 ns, the delay PDF within 0–2500 ns is given in Fig. 12. As we can see that it obeys the exponential distribution, which is also reasonable according to the generation method of (12). It should be mentioned that the largest delay in the simulations could be much larger than 2500 ns, e.g., over 40000 ns, but the probability is extremely small.

For the case of NLOS scenario, a series of simulations are also performed and the results are given in Fig. 13. Two simulation results of PDP are given in Fig. 13(a) and Fig. 13(b), respectively. The simulated mean PDP is shown in Fig. 14, which fits well with the exponential model with respect to the delay. In Fig. 15, the simulated PDF of the delay over 0–5000 ns also obeys the exponential distribution well. It should be mentioned that the simulated CDF of delay is over 95% when the delay equals 5000 ns in the NLOS scenario. In another word, the delay in the NLOS scenario has a much wider range than the one in the LOS scenario.

### 3) Angle parameters:

The composite power angular spectrum (PAS) in the azimuth plane is modeled as a wrapped Gaussian distribution in the 3GPP channel model [54], [71]. The azimuth angles of arrival (AOAs) can be obtained by using the inverse Gaussian function as

$$\varphi'_{n,AOA} = \frac{2(ASA/1.4)\sqrt{-\ln(P_n/\max(P_n))}}{C_\varphi} \quad (18)$$

where  $ASA$  is the azimuth angle spread of arrival and  $C_\varphi$  is a measurement-based factor and dependent on the total number of clusters for NLOS components. For the LOS case, the first cluster should be enforced to the LOS direction by adding an offset to all cluster

angles. The final angles within each cluster can be generated by

$$\varphi_{n,m,AOA} = \varphi_{n,AOA} + c_{ASA}\alpha_m \quad (19)$$

where  $\varphi_{n,AOA}$  is obtained by introducing random variables in  $\varphi'_{n,AOA}$ ,  $c_{ASA}$  is the azimuth angle spread, and  $\alpha_m$  is the ray offset angle with normalized angle spread defined in Table VII. The generation method of azimuth angle of departure (AOD) is similar to the one of AOA.

The composite PAS in zenith plane is modeled as Laplacian in the 3GPP channel model. The zenith angle of arrival (ZOA) can be obtained by using the inverse Laplacian function as

$$\theta'_{n,ZOA} = -\frac{ZSA \ln(P_n / \max(P_n))}{C_\theta} \quad (20)$$

where  $ZSA$  is the zenith angle spread of arrival, and  $C_\theta$  is a measurement-based factor and also dependent on the total number of clusters for NLOS components. For the LOS case, the first cluster should be enforced to the LOS direction by adding an offset to all cluster angles. The final angles within each cluster can be generated by

$$\theta_{n,m,ZOA} = \theta_{n,ZOA} + c_{ZSA}\alpha_m \quad (21)$$

where  $\varphi_{n,ZOA}$  is obtained by introducing random variables in  $\varphi'_{n,ZOA}$ ,  $c_{ZSA}$  is the zenith angle spread, and  $\alpha_m$  is the ray offset angle with normalized angle spread. Note that  $\theta_{n,m,ZOA}$  is wrapped within  $[0, 360^\circ]$  while  $\theta_{n,ZOA}$  is defined within  $[0, 180^\circ]$ . Therefore, if  $\theta_{n,m,ZOA} \in [180^\circ, 360^\circ]$ ,  $\theta_{n,m,ZOA}$  should be set to  $(360^\circ - \theta_{n,m,ZOA})$ . The generation method of zenith angle of departure (ZOD) is similar to the one of ZOA.

Finally, AOD and AOA angles are paired randomly within each cluster or a sub-cluster for the two strongest clusters. The same coupling method can be used for the ZODs and ZOAs.

Based on parameters given in Table VIII, a series of simulations are carried out to illustrate the properties of AOAs and ZOAs. For the NLOS case, the angular distributions of four different clusters in the a simulation are generated and shown in Fig. 16, where AOA denotes the azimuth angle of arrival, and ZOA denotes the zenith angle of arrival. The triangle marks in the figure represent angular conditions of the cluster, while the

round marks represent the angular conditions of the ray in the cluster. It can be seen that the mark of the cluster is centered around the marks of the rays in each sub-figure due to the approaches mentioned above. Fig. 17 shows the angular distribution of eight different clusters in one simulation. Note that the azimuth angle of arrival ranges from 0 to 360 degrees, and the zenith angle of arrival ranges from 0 to 180 degrees. It is obvious that the angular distribution of different clusters is of huge distinction, which is caused by direction, reflection and diffraction of the signals.

### III. MAP-BASED HYBRID CHANNEL MODEL

#### A. Framework

The 3GPP map-based hybrid channel model can be used to evaluate or predict system performance when the detailed digital map is known and the impacts of environmental structures and materials are required to be taken into account. It consists of a deterministic component generated by the RT method and a stochastic component generated by the approaches described in the previous sections as shown in Fig. 18. Note that the hybrid model defined by 3GPP is not calibrated. Some details of modeling procedure will be demonstrated and analyzed in the following.

#### B. Digital map reconstruction

To build a map-based hybrid channel model, it is essential to calculate the channel parameters according to the realistic propagation environment. Actually, the model parameters can be created by using the RT method upon the digitized map with some certain stochastic components [72], [73]. The RT techniques have been widely used for the propagation modeling since the 90's. It describes all possible propagation paths by huge number of rays which may be reflected on the scatterer surfaces and diffracted on the scatterer wedges. It has been applied in channel modelling under different scenarios, e.g., indoor [81], urban [82], [83], metro tunnel [84], [85], air-to-ground [86], and marine [87].

The shortcoming of RT method is the high computation complexity and request for accurate description of scattering environments. The description is stored in a database

and usually has a huge volume due to the geometric and physical complexity of scattering environments [74]. The procedure of tracking all the rays often needs extremely large computation time dependent on the size of database. Therefore, it is an efficient way to reduce the time consumption by simplifying the database with losing little accuracy. For example, by only considering the main geometric scatterers (or the main rays), the authors in [75] proposed a simplified algorithm to improve the efficiency of mmWave channel modeling. The detailed process to reconstruct the database of terrain and buildings in [75] is introduced as follow.

Firstly, original map of the interesting area in the form of digital terrain model (DEM) is needed. It has detailed information of latitude, longitude, and elevation of all points, which can be used to reconstruct many triangle facets to approximately describe the surface of terrain. Secondly, buildings with complex structures, which are obtained from satellite maps, can be approximated by uniform structures with flat tops. On this basis, the height information is used to construct the 3D database and be superimposed on the terrain. An example of reconstructed digital map including the terrain, buildings, and vegetation is shown in Fig. 19. Note that when the large terrain with buildings and vegetation is taken into account, the triangle facets may no longer be regular ones in order to connect with all scatterers. In addition, the reconstruction is flexible to achieve the tradeoff between complexity and accuracy.

### *C. RT method application*

The RT method is based on the geometrical theory of diffraction, uniform theory of diffraction, and field intensity superposition principle [76]–[78]. By using the forward or reverse tracking techniques, channel parameters, i.e., electric field intensity or amplitude, delay, phase, and angle of each ray, can be analyzed and obtained [79], [80].

In addition, the RT method has great applicability for the high frequency bands and is supposed to be the most accurate and versatile analytical approach for mmWave propagation prediction [88]–[96]. For instance, the authors in [94] analyzed channel model parameters by assigning different materials in an indoor environment by RT simulations. The diffuse multipath components were combined with the specular component to obtain a complete channel representation in [95]. Moreover, the accuracy of RT method was

validated under a 3D environment model with proper material electromagnetic parameters in [96].

To illustrate the procedure of generating deterministic component, a simple instance is presented in the following. A typical indoor environment with Tx and Rx at different locations is reconstructed, and the geometric calculations are performed to identify propagation interaction types, including the direction, reflections, diffractions, and penetrations. According to the 3GPP recommendations, the maximum order of reflection on a path without diffraction is configurable from  $\{1, 2, 3\}$ , the maximum order of diffraction on a path without reflection is configurable from  $\{1, 2\}$ , the path containing both reflection and diffraction has 1-order reflection and 1-order diffraction besides any potential penetrations, and the maximum order of penetration on a path is configurable with the recommended value equal to 5.

Since the electromagnetic propagation process can be divided into three cases, different methods are needed to calculate the corresponding electric field intensity. For the directed ray (or LOS ray), the electric field intensity can be calculated by

$$E_0(t) = E^{1m} \frac{e^{-jk d_0^{tx}(t)}}{d_0^{tx}(t)} \quad (22)$$

where  $E^{1m}$  is the electric field intensity at a distance of 1 m from the Tx,  $k$  is the wave number and  $d_0^{tx}(t)$  is the distance between the Tx and Rx. For the reflected rays, the calculation formula of electric field intensity can be described as

$$E_l^R(t) = E_0 R \frac{e^{-jk(d_l^{tx,S}(t) + d_l^{S,Rx}(t))}}{d_l^{tx,S}(t) + d_l^{S,Rx}(t)} \quad (23)$$

where  $R$  is the reflection coefficient,  $d_l^{tx,S}(t)$  is the distance between the Tx and scatterer and  $d_l^{S,Rx}(t)$  is the distance between the Rx and scatterer.

For the diffracted rays, the electric field intensity can be expressed as

$$E_l^D(t) = \frac{E_0}{d_l^{S,Rx}(t)} D \sqrt{\frac{d_l^{S,Rx}(t)}{d_l^{tx,S}(t) \cdot (d_l^{tx,S}(t) + d_l^{S,Rx}(t))}} \cdot e^{-jk(d_l^{tx,S}(t) + d_l^{S,Rx}(t))} \quad (24)$$

where  $D$  is the diffraction coefficient.

The simulations are carried out and the schematic is shown in Fig. 20. It can be found that both the maximum diffraction order and the maximum reflection order are set to 2.



When the reflection and diffraction exist at the same time, both their orders are set to 1. Note that each simulation contains all rays, but only the rays that contribute to the electric field strength on the receiving point are chosen and tracked.

In order to observe powers and delays of different propagation paths, Fig. 21 shows the simulated PDP where the Tx located at Tx1, and the three Rxs located at Rx1, Rx2, and Rx3, respectively. In the simulation, the frequency is set to 60 GHz, the bandwidth to 50 MHz, and the transmitting power to 30 dBm. The Tx and Rxs are all equipped with omnidirectional horn antennas. The height of Tx antenna is 0.8 m, the heights of Rx antennas are 0.8 m, 0.5 m, and 0.5 m respectively. It can be found that the power of the signal received by Rx1 is significantly higher than others due to the LOS path between Tx1 and Rx1, and the power of 1-order diffraction is higher than that of 2-order diffraction while the delay is smaller. In addition, the received power which experiences the 1-order reflection is higher than the 2-order reflection under the propagation between the Tx1 and Rx2. For Tx1 and Rx3, the received power which goes through 1-order diffraction is higher than the 1-order reflection due to the path length.

#### IV. CONCLUSIONS

This chapter has illustrated the generation procedure of 3GPP channel model in TR 38.901 which includes two kind of channel models, i.e., the stochastic model and the map-based model. The 3GPP stochastic channel model contains two parts such as the large-scale fading and the small-scale fading. For the large-scale fading, the calculation method of path loss, penetration loss, and oxygen loss has been summarized and simulated to demonstrate how these factors affect the received power. Furthermore, a series of simulations for the small-scale fading parameters, i.e., path delay, path power, and angle have also been carried out to illustrate the statistical properties and relationships between these parameters under different scenarios. Finally, a framework of 3GPP map-based hybrid channel model and some modeling principles have been illustrated. An example of RT method under indoor scenario has been given to demonstrate the generation procedure of deterministic component in the map-based hybrid channel model.

## V. ACKNOWLEDGEMENT

This work was supported by the National Key R&D Program of China under Grant 2018YFB1801101, the National Key Scientific Instrument and Equipment Development Project under Grant 61827801, the National Natural Science Foundation of China under Grant 61960206006, the Frontiers Science Center for Mobile Information Communication and Security, the High Level Innovation and Entrepreneurial Research Team Program in Jiangsu, the High Level Innovation and Entrepreneurial Talent Introduction Program in Jiangsu, the Aeronautical Science Foundation of China under Grant 201901052001, the Fundamental Research Funds for the Central Universities under Grant NS2020026 and 2242020R30001, the Huawei Cooperation Project, and the EU H2020 RISE TESTBED2 project under Grant 872172.

## REFERENCES

- [1] C.-X. Wang, J. Bian, J. Sun, W. Zhang, and M. Zhang, "A survey of 5G channel measurements and models," *IEEE Commun. Surveys Tuts.*, vol. 20, no. 4, pp. 3142–3168, Aug. 2018.
- [2] P. Zhang, X. Yang, J. Chen and Y. Huang, "A survey of testing for 5G: Solutions, opportunities, and challenges," *China Commun.*, vol. 16, no. 1, pp. 69–85, Jan. 2019.
- [3] A. N. Uwaechia and N. M. Mahyuddin, "A comprehensive survey on millimeter wave communications for fifth-generation wireless networks: Feasibility and challenges," *IEEE Access*, vol. 8, pp. 62367–62414, Mar. 2020.
- [4] W. Fan, I. Carton, P. Kyosti, A. Karstensen, T. Jamsa, et al., "A step toward 5G in 2020: low-cost OTA performance evaluation of massive MIMO base stations," *IEEE Antennas Propag. Mag.*, vol. 59, no. 1, pp. 38–47, Feb. 2017.
- [5] J. Zhang, M. Shafi, A. F. Molisch, F. Tufvesson, S. Wu and K. Kitao, "Channel models and measurements for 5G," *IEEE Commun. Mag.*, vol. 56, no. 12, pp. 12–13, Dec. 2018.
- [6] M. K. Samimi and T. S. Rappaport, "3-D millimeter-wave statistical channel model for 5G wireless system design," *IEEE Trans. Microw. Theory Tech.*, vol. 64, no. 7, pp. 2207–2225, July 2016.
- [7] S. Hur, S. Baek, B. Kim, Y. Chang, A. F. Molisch, T. S. Rappaport, K. Haneda, and J. Park, "Proposal on millimeter-wave channel modeling for 5G cellular system," *IEEE J. Sel. Top. Signal Process.*, vol. 10, no. 3, pp. 454–469, Apr. 2016.
- [8] G. Yang, Y. Zhang, Z. He, J. Wen, Z. Ji, et al., "Machine-learning-based prediction methods for path loss and delay spread in air-to-ground millimeter-wave channels," *IET Microw. Antennas Propag.*, vol. 13, no. 8, pp. 1113–1121, June 2019.
- [9] P. Alberto, A. Fouda, and A. S. Ibrahim. "Ray tracing analysis for UAV-assisted integrated access and backhaul millimeter wave networks," in *Proc. WoWMoM'19*, Washington, DC, USA, Aug. 2019.
- [10] Z. Cui, K. Guan, D. He, B. Ai, and Z. Zhong, "Propagation modeling for UAV air-to-ground channel over the simple mountain terrain," in *Proc. ICC Workshops'19*, Shanghai, China, July 2019.

- [11] W. Khawaja, O. Ozdemir and I. Guvenc, "Temporal and spatial characteristics of mm wave propagation channels for UAVs," in *Proc. GSMM'18*, Boulder, CO, USA, May 2018.
- [12] X. Chu, C. Briso, D. He, X. Yin, and J. Dou, "Channel modeling for low-altitude UAV in suburban environments based on ray tracer," in *Proc. EuCAP'18*, London, UK, Apr. 2018.
- [13] Z. Liu, D. Shi, Y. Gao, C. Yuan, J. Bi, et al., "A new ray tracing acceleration technique in the simulation system of electromagnetic situation," in *Proc. CEEM'15*, Hangzhou, China, Nov. 2015.
- [14] L. Cheng, Q. Zhu, C.-X. Wang, W. Zhong, B. Hua, et al., "Modeling and simulation for UAV air-to-ground mmWave channels," in *Proc. EuCAP'20*, Copenhagen, Denmark, Mar. 2020.
- [15] S. Salous, V. D. Esposti, F. Fuschini, R. S. Thomae, R. Mueller, D. Dupleich, et al., "Millimeter-Wave Propagation: Characterization and modeling toward fifth-generation systems. [Wireless Corner]," *IEEE Antennas Propag. Mag.*, vol. 58, no. 6, pp. 115–127, Dec. 2016.
- [16] J. Järveläinen, K. Haneda and A. Karttunen, "Indoor propagation channel simulations at 60 GHz using point cloud data," *IEEE Trans. Antennas Propag.*, vol. 64, no. 10, pp. 4457–4467, Oct. 2016.
- [17] X. Wu, C.-X. Wang, J. Sun, J. Huang, R. Feng, Y. Yang, et al., "60-GHz millimeter-wave channel measurements and modeling for indoor office environments," *IEEE Trans. Antennas Propag.*, vol. 65, no. 4, pp. 1912–1924, Apr. 2017.
- [18] A. A. M. Saleh and R. Valenzuela, "A statistical model for indoor multipath propagation," *IEEE J. Sel. Areas Commun.*, vol. 5, no. 2, pp. 128–137, Feb. 1987.
- [19] J. Huang, C. Wang, R. Feng, J. Sun, W. Zhang and Y. Yang, "Multi-frequency mmWave massive MIMO channel measurements and characterization for 5G wireless communication systems," *IEEE J. Sel. Areas Commun.*, vol. 35, no. 7, pp. 1591–1605, July 2017.
- [20] H. Chang, J. Bian, C.-X. Wang, Z. Bai, W. Zhou and e. M. Aggoune, "A 3D non-stationary wideband GBSM for low-altitude UAV-to-ground V2V MIMO channels," *IEEE Access*, vol. 7, pp. 70719–70732, May 2019.
- [21] H. Jiang, Z. Zhang and G. Gui, "A novel estimated wideband geometry-based vehicle-to-vehicle channel model using an AoD and AoA estimation algorithm," *IEEE Access*, vol. 7, pp. 35124–35131, Feb. 2019.
- [22] W. Li, X. Chen, Q. Zhu, W. Zhong, D. Xu and F. Bai, "A novel segment-based model for non-stationary vehicle-to-vehicle channels with velocity variations," *IEEE Access*, vol. 7, pp. 133442–133451, Sept. 2019.
- [23] X. Zhao, F. Du, S. Geng, N. Sun, Y. Zhang, Z. Fu, et al., "Neural network and GBSM based time-varying and stochastic channel modeling for 5G millimeter wave communications," *China Commun.*, vol. 16, no. 6, pp. 80–90, June 2019.
- [24] Q. Zhu, H. Li, Y. Fu, C.-X. Wang, Y. Tan, et al., "A novel 3D nonstationary wireless MIMO channel simulator and hardware emulator," *IEEE Trans. Commun.*, vol. 66, no. 9, pp. 3865–3878, Sept. 2018.
- [25] A. Al-Kinani, J. Sun, C.-X. Wang, W. Zhang, X. Ge, and H. Haas, "A 2-D non-stationary GBSM for vehicular visible light communication channels," *IEEE Trans. Wirel. Commun.*, vol. 17, no. 12, pp. 7981–7992, Oct. 2018.
- [26] C. A. Gutierrez, J. T. Gutierrez-Mena, J. M. Luna-Rivera, D. U. Campos-Delgado, R. Velazquez, and M. Patzold, "Geometry-based statistical modeling of non-WSSUS mobile-to-mobile rayleigh fading channels," *IEEE Trans. Vehi. Tech.*, vol. 67, no. 1, pp. 362–377, Jan. 2018.
- [27] E. T. Michailidis, N. Nomikos, P. Trakadas, and A. G. Kanatas, "Three-dimensional modeling of mmWave doubly massive MIMO aerial fading channels," *IEEE Trans. Vehi. Tech.*, vol. 69, no. 2, pp. 1190–1202, Feb. 2020.
- [28] J. Huang, Y. Liu, C.-X. Wang, J. Sun, and H. Xiao, "5G millimeter wave channel sounders, measurements,

- and models: Recent developments and future challenges,” *IEEE Commun. Mag.*, vol. 57, no. 1, pp. 138–145, Jan. 2019.
- [29] X. Zhao, F. Du, S. Geng, Z. Fu, Z. Wang, Y. Zhang, et al., “Playback of 5G and beyond measured MIMO channels by an ANN-based modeling and simulation framework,” *IEEE J. Sel. Areas Commun.*, early access, June 2020.
- [30] C. U. Bas, R. Wang, S. Sangodoyin, S. Hur, K. Whang, J. Park, et al., “28 GHz propagation channel measurements for 5G microcellular environments,” in *Proc. ACES’18*, Denver, CO, 2018.
- [31] X. Zhao, S. Li, Q. Wang, M. Wang, S. Sun and W. Hong, “Channel measurements, modeling, simulation and validation at 32 GHz in outdoor microcells for 5G radio systems,” *IEEE Access*, vol. 5, pp. 1062–1072, Jan. 2017.
- [32] J. Ko, Y. Cho, S. Hur, T. Kim, J. Park, A. F. Molisch, et al., “Millimeter-wave channel measurements and analysis for statistical spatial channel model in in-building and urban environments at 28 GHz,” *IEEE Trans. Wirel. Commun.*, vol. 16, no. 9, pp. 5853–5868, Sept. 2017.
- [33] C. U. Bas, R. Wang, S. Sangodoyin, S. Hur, K. Whang, J. Park, et al., “28 GHz microcell measurement campaign for residential environment,” in *Proc. GLOBECOM’17*, Singapore, Dec. 2017.
- [34] 3GPP TR. 38.901, *Study on channel model for frequencies from 0.5 to 100 GHz, V16.1.0*, Jan. 2020.
- [35] S. Jaeckel, L. Raschkowski, K. Börner, L. Thiele, F. Burkhardt and E. Eberlein, *QuaDRiGa – quasi deterministic radio channel generator; user manual and documentation, v2.2.0*, Fraunhofer Heinrich Hertz Institute, Tech. Rep., 2019
- [36] S. Jaeckel, N. Turay, L. Raschkowski, L. Thiele, R. Vuoltoniemi, et al., “Industrial indoor measurements from 2-6 GHz for the 3GPP-NR and QuaDRiGa channel model,” in *Proc. IEEE VTC-Fall’19*, Honolulu, HI, USA, 2019.
- [37] S. Jaeckel, L. Raschkowski, K. Börner and L. Thiele, “QuaDRiGa: A 3-D multi-cell channel model with time evolution for enabling virtual field trials,” in *IEEE Trans. Antennas Propag.*, vol. 62, no. 6, pp. 3242–3256, June 2014.
- [38] Int. Telecommun. Union, *IMT-2020 Preliminary Draft New Report ITU-R M.[IMT-2020.EVAL]*, document R15-WP5D-170613-TD-0332, Niagara Falls, ON, Canada, June 2017.
- [39] mmMAGIC, *Measurement results and final mmMAGIC channel models, v1*, Rep. H2020-ICT-671650-mmMAGIC/D2.2, Dec. 2017.
- [40] A. Maltsev et al., *Channel Models for IEEE 802.11ay*, document 802.11-15/1150r9, IEEE, New York, NY, USA, 2016.
- [41] V. Nurmela et al., *METIS Channel Models*, document ICT-317669/D1.4, METIS, New York, NY, USA, July 2015.
- [42] A. Maltsev et al., *Channel Modeling and Characterization, V1.0*, document FP7-ICT-608637/D5.1, MiWEBA, Breitengußbach, Germany, Jun. 2014.
- [43] A. Maltsev, A. Pudseyev, I. Karls, I. Bolotin, G. Morozov, R. Weiler, et al., “Quasi-deterministic approach to mmWave channel modeling in a non-stationary environment,” in *Proc. IEEE GC Wkshps’14*, Austin, TX, USA, 2014.
- [44] 5GCMSIG, *5G channel model for bands up to 100 GHz, v2.0*, Aalto Univ., Espoo, Finland, White Paper, Mar. 2014.
- [45] L. Liu, C. Oestges, J. Poutanen, K. Haneda, P. Vainikainen, F. Quitin, et al., “The COST 2100 MIMO channel model,” *IEEE Wirel. Commun.*, vol. 19, no. 6, pp. 92–99, Dec. 2012.

- [46] R. Verdone and A. Zanella, *Pervasive Mobile and Ambient Wireless Communications*. London, U.K.: Springer, 2012.
- [47] 3rd Generation Partnership Project, Technical Specification Group Radio Access Network, *Spatial channel model for MIMO simulations, V6.1.0*, 2003.
- [48] IST-4-027756 WINNER II (2003), *D1.1.1 WINNER II interim channel models, v1.0*, Dec. 2006.
- [49] J. Medbo, K. Börner, K. Haneda, V. Hovinen, T. Imai, J. Järveläinen, et al., “Channel modeling for the fifth generation mobile communications,” in *Proc. EuCAP’14*, The Hague, The Netherlands, 2014.
- [50] Y. Yang, J. Xu, G. Shi, and C.-X. Wang, Ed., “*5G Wireless Systems*”, Chippenham: Springer, Oct. 2017.
- [51] M. Rumney, K. Technologies, P. Kyosti, and L. Hentila, “3GPP channel model developments for 5G NR requirements and testing,” in *Proc. EuCAP’18*, London, UK, Apr. 2018.
- [52] S. Wu, C.-X. Wang, H. Aggoune, M. M. Alwakeel, and X. You, “A general 3D non-stationary 5G wireless channel model,” *IEEE Trans. Commun.*, vol. 66, no. 7, pp. 3065–3078, July 2018.
- [53] Y. Zhang, A. Ghazal, C.-X. Wang, H. Zhou, W. Duan, and H. Aggoune, “Accuracy-complexity tradeoff analysis and complexity reduction methods for non-stationary IMT-A MIMO channel models,” *IEEE Access*, vol. 7, no. 1, pp. 178047–178062, Dec. 2019.
- [54] B. Mondal, T. A. Thomas, E. Visotsky, F. W. Vook, A. Ghosh, et al., “3D channel model in 3GPP,” *IEEE Commun. Mag.*, vol. 53, no. 3, pp. 16–23, Mar. 2015.
- [55] M. Narandzic, C. Schneider, R. Thoma, T. Jamsa, P. Kyosti, and X. Zhao, “Comparison of SCM, SCME, and WINNER channel models,” in *Proc. IEEE VTC’07*, Dublin, Ireland, Apr. 2007.
- [56] C.-X. Wang, X. Hong, H. Wu, and W. Xu, “Spatial temporal correlation properties of the 3GPP spatial channel model and the Kronecker MIMO channel model,” *EURASIP J. Wireless Commun. Netw.*, vol. 2007, pp. 1–9, Jan. 2007.
- [57] V. V. Díaz and D. Marciano Aviles, “A Path Loss Simulator for the 3GPP 5G Channel Models,” in *Proc. IEEE XXV INTERCON’18*, Lima, Peru, Aug. 2018.
- [58] K. Guan, G. Li, D. He, L. Wang, B. Ai, R. He, et al., “Spatial consistency of dominant components between ray-tracing and stochastic modeling in 3GPP high-speed train scenarios,” in *Proc. EuCAP’17*, Paris, France, Mar. 2017.
- [59] M. K. Samimi and T. S. Rappaport, “Local multipath model parameters for generating 5G millimeter-wave 3GPP-like channel impulse response,” in *Proc. EuCAP’16*, Davos, Switzerland, Mar. 2016.
- [60] Z. Cui, K. Guan, C. Briso-Rodriguez, B. Ai, and Z. Zhong, “Frequency-dependent line-of-sight probability modeling in built-up environments,” *IEEE Internet Things J.*, vol. 7, no. 1, pp. 699–709, Jan. 2020.
- [61] T. S. Rappaport, Y. Xing, G. R. MacCartney, A. F. Molisch, E. Mellios, and J. Zhang, “Overview of millimeter wave communications for fifth-generation (5G) wireless networks-With a focus on propagation models,” *IEEE Trans. Antennas Propag.*, vol. 65, no. 12, pp. 6213–6230, Dec. 2017.
- [62] M. K. Samimi, T. S. Rappaport, and G. R. MacCartney, “Probabilistic omnidirectional path loss models for millimeter-wave outdoor communications,” *IEEE Wireless Commun. Lett.*, vol. 4, no. 4, pp. 357–360, Aug. 2015.
- [63] ITU-R, “Rec. P.1410-2 Propagation data and prediction methods for the design of terrestrial broadband millimetric radio access systems,” *P Series, Radiowave propagation*, 2003.
- [64] G. R. MacCartney, and T. S. Rappaport, “Rural macrocell path loss models for millimeter wave wireless communications,” *IEEE J. Sel. Areas Commun.*, vol. 35, no. 7, pp. 1663–1677, July 2017.

- [65] A. Al-Hourani, and K. Gomez, "Modeling cellular-to-UAV path-loss for suburban environments," *IEEE Wireless Commun. Lett.*, vol. 7, no. 1, pp. 82–85, Feb. 2018.
- [66] A. I. Sulyman, A. Alwarafy, G. R. MacCartney, T. S. Rappaport, and A. Alsanie, "Directional radio propagation path loss models for millimeter-wave wireless networks in the 28-, 60-, and 73-GHz bands," *IEEE Trans. Wireless Commun.*, vol. 15, no. 10, pp. 6939–6947, Oct. 2016.
- [67] S. Sun, T. S. Rappaport, T. A. Thomas, A. Ghosh, H. C. Nguyen, I. Z. Kovacs, I. Rodriguez, O. Koymen, and A. Partyka, "Investigation of prediction accuracy, sensitivity, and parameter stability of large-scale propagation path loss models for 5G wireless communications," *IEEE Trans. Vehi. Tech.*, vol. 65, no. 5, pp. 2843–2860, May 2016.
- [68] G. R. Maccartney, T. S. Rappaport, S. Sun, and S. Deng, "Indoor office wideband millimeter-wave propagation measurements and channel models at 28 and 73 GHz for ultra-dense 5G wireless networks," *IEEE Access*, vol. 3, no. 1, pp. 2388–2424, Oct. 2015.
- [69] T. Jost, W. Wang, and M. Walter, "A geometry-based channel model to simulate an averaged-power-delay profile," *IEEE Trans. Antennas Propag.*, vol. 65, no. 9, pp. 4925–4930, Sept. 2017.
- [70] M. Zhang, M. Polese, M. Mezzavilla, S. Rangan, and M. Zorzi, "ns-3 implementation of the 3GPP MIMO channel model for frequency spectrum above 6 GHz," in *Proc. WNS-3'17*, New York, United States, June 2017.
- [71] S. L. H. Nguyen, J. Jarvelainen, A. Karttunen, K. Haneda, and J. Putkonen, "Comparing radio propagation channels between 28 and 140 GHz bands in a shopping mall," in *Proc. EuCAP'18*, London, UK, Apr. 2018.
- [72] V. Degli-Esposti, F. Fuschini, E. M. Vitucci, and G. Falciasecca, "Speedup techniques for ray tracing field prediction models," *IEEE Trans. Antennas Propag.*, vol. 57, no. 5, pp. 1469–1480, May 2009.
- [73] V. K. Aleksey, V. N. Andrey, and V. A. Vadim, "The algorithm for calculating reflecting signal power characteristics based on terrain digital map," in *Proc. IEEE EDM'17*, Erlagol, Russia, July 2017.
- [74] Q. Zhu, S. Jiang, C.-X. Wang, B. Hua, K. Mao, et al., "Effects of digital map on the RT-based channel model for UAV mmWave communications," in *Proc. IWCMC'20*, Limassol, Cyprus, June 2020.
- [75] S. Jiang, Q. Zhu, C.-X. Wang, K. Mao, W. Xie, et al., "Map-based UAV mmWave channel model and characteristic analysis," in *Proc. ICC'20*, Chongqing, China, Aug. 2020.
- [76] P. D. Holm, "A new heuristic UTD diffraction coefficient for nonperfectly conducting wedges," *IEEE Trans. Antennas Propag.*, vol. 48, no. 8, pp. 1211–1219, Aug. 2000.
- [77] Z. Yun, and M. F. Iskander, "Ray tracing for radio propagation modeling: Principles and applications," *IEEE Access*, vol. 3, pp. 1089–1100, Aug. 2015.
- [78] Y. Wu, Z. Gao, C. Chen, L. Huang, and H. Chiang, "Ray tracing based wireless channel modeling over the sea surface near diaoyu islands," in *Proc. CCITSA'15*, Yilan, Taiwan, Dec. 2015.
- [79] G. E. Athanasiadou, and A. R. Nix, "A novel 3-D indoor ray-tracing propagation model: the path generator and evaluation of narrow-band and wide-band predictions," *IEEE Trans. Vehic. Technol.*, vol. 49, no. 4, pp. 1152–1168, July 2000.
- [80] C.-F. Yang, B.-C. Wu, and C.-J. Ko, "A ray-tracing method for modeling indoor wave propagation and penetration," *IEEE Trans. Antennas Propag.*, vol. 46, no. 6, pp. 907–919, June 1998.
- [81] S. Chamaani, S. A. Mirtaheri, Y. I. Nechayev and P. S. Hall, "MICS band indoor channel modeling using ray tracing method," in *Proc. ISTEL'10*, Tehran, Iran, Dec. 2010.
- [82] D. N. Schettino, F. J. S. Moreira and C. G. Rego, "Efficient ray tracing for radio channel characterization of urban scenarios," *IEEE Trans. Magn.*, vol. 43, no. 4, pp. 1305–1308, Apr. 2007.

- [83] S. Yang, J. Zhang and J. Zhang, "Impact of foliage on urban mmWave wireless propagation channel: A ray-tracing based analysis," in *Proc. ISAP'19*, Xi'an, China, Oct. 2019.
- [84] B. Choudhury and R. M. Jha, "A refined ray tracing approach for wireless communications inside underground mines and metrorail tunnels," in *Proc. AEMC'11*, Kolkata, India, Dec. 2011.
- [85] C. Zheng, Z. Xu, D. He, K. Guan, B. Ai and J. M. García-Loygorri, "Millimeter-Wave Channel Measurement Based Ray-Tracing Calibration and Analysis in Metro," in *Proc. ISAP'19*, Atlanta, GA, USA, July 2019.
- [86] C. Calvo-Ramírez, Z. Cui, C. Briso, K. Guan and D. W. Matolak, "UAV Air-Ground Channel Ray Tracing Simulation Validation," in *Proc. ICCCW'18*, Beijing, China, Aug. 2018.
- [87] Z. Gao, B. Liu, Z. Cheng, C. Chen and L. Huang, "Marine mobile wireless channel modeling based on improved spatial partitioning ray tracing," *China Commun.*, vol. 17, no. 3, pp. 1–11, Mar. 2020.
- [88] S. Sasmal, S. Mishra, B. R. Behera and S. Bandopadhyaya, "Ray tracing channel model for millimeter-(mm-) wave systems," in *Proc. ICACCT'16*, Ramanathapuram, India, May 2016.
- [89] D. He, B. Ai, K. Guan, L. Wang, Z. Zhong and T. Kurner, "The design and applications of high-performance ray-tracing simulation platform for 5G and beyond wireless communications: A tutorial," *IEEE Commun. Surveys Tuts.*, vol. 21, no. 1, pp. 10–27, Aug. 2018.
- [90] J. Pascual-Garcia, M. Martinez-Ingles, J. M. Garcia-Pardo, J. Rodriguez and L. J. Llaser, "Using tuned diffuse scattering parameters in ray tracing channel modeling," in *Proc. EuCAP'15*, Lisbon, Portugal, Apr. 2015.
- [91] M. Jung, J. H. Kim, J. S. Kim, W. H. Jeong, and K. Kim, "The path loss characteristics for new wireless mobile communication system in outdoor environments," in *Proc. EuMC'12*, Amsterdam, Netherlands, Nov. 2012.
- [92] T. Kurner and M. Jacob, "Application of ray tracing to derive channel models for future multi-gigabit systems," in *Proc. ICEAA'09*, Torino, Italy, Sept. 2009.
- [93] M. Peter, W. Keusgen and R. Felbecker, "Measurement and ray-tracing simulation of the 60 GHz indoor broadband channel: Model accuracy and parameterization," in *Proc. EuCAP'07*, Edinburgh, UK, Nov. 2007.
- [94] J. Pascual-Garcia, J. Molina-Garcia-Pardo, M. Martinez-Ingles, J. Rodriguez and N. Saurin-Serrano, "On the importance of diffuse scattering model parameterization in indoor wireless channels at mm-Wave frequencies," *IEEE Access*, vol. 4, pp. 688–701, Feb. 2016.
- [95] L. Tian, V. Degli-Esposti, E. M. Vitucci and X. Yin, "Semi-deterministic radio channel modeling based on graph theory and ray-tracing," *IEEE Trans. Antennas Propag.*, vol. 64, no. 6, pp. 2475–2486, June 2016.
- [96] A. Zhou, J. Huang, J. Sun, Q. Zhu, C.-X. Wang and Y. Yang, "60 GHz channel measurements and ray tracing modeling in an indoor environment," in *Proc. ICWCSP'17*, Nanjing, China, Oct. 2017.

## VI. FURTHER READING/RESOURCES

- 1) C.-X. Wang, X. Hong, H. Wu, and W. Xu, "Spatial-temporal correlation properties of the 3GPP spatial channel model and the kronecker MIMO channel model," *EURASIP J. Wirel. Commun. Netw.*, vol. 2007, no. 1, pp. 39871–39879, Feb. 2007.
- 2) H. Xiao, A. G. Burr, and R. C. d. Lamare, "Reduced-complexity cluster modelling for the 3GPP channel model," in *Proc. IEEE ICC'07*, Glasgow, Scotland, UK, June 2007.
- 3) M. Narandzic, C. Schneider, R. Thoma, T. Jamsa, P. Kyosti and X. Zhao, "Comparison of SCM, SCME, and WINNER channel models," in *Proc. IEEE VTC-Spring'07*, Dublin, Ireland, Apr. 2007.
- 4) J. Medbo, M. Riback and J. -. Berg, "Validation of 3GPP spatial channel model including WINNER wideband extension using measurements," in *Proc. IEEE VTC-Fall'06*, Montreal, Que., Canada, Sept. 2006.
- 5) R. Almesaeed, A. S. Ameen, E. Mellios, A. Doufexi, and A. R. Nix, "A proposed 3D extension to the 3GPP/ITU channel model for 800 MHz and 2.6 GHz bands," in *Proc. EuCAP'14*, The Hague, Netherlands, Apr. 2014.
- 6) F. Ademaj, M. Taranetz, and M. Rupp, "Implementation, validation and application of the 3GPP 3D MIMO channel model in open source simulation tools," in *Proc. ISWCS'15*, Brussels, Belgium, Aug. 2015.
- 7) N. Nguyen, B. Tran, and V. D. Nguyen, "A code scheme SFBC on 3GPP channel model in correlated MIMO-OFDMA system," *Proc. ICATC'14*, Hanoi, Vietnam, Oct. 2014.
- 8) B. Mondal et al., "3D channel model in 3GPP," *IEEE Commun. Mag.*, vol. 53, no. 3, pp. 16–23, Jan. 2015.
- 9) S. A. Busari, K. M. S. Huq, S. Mumtaz, and J. Rodriguez, "Impact of 3D channel modeling for ultra-high speed beyond-5G networks," in *Proc. IEEE GC Wkshps'18*, Abu Dhabi, United Arab Emirates, Dec. 2018.
- 10) S. Jaeckel, L. Raschkowski, F. Burkhardt and L. Thiele, "Efficient sum-of-sinusoids-based spatial consistency for the 3GPP new-radio channel model," in *Proc. IEEE GC Wkshps'18*, Abu Dhabi, United Arab Emirates, Dec. 2018.



- 11) X. Ge, Y. Qiu, J. Cheng, M. Huang, H. Xu, J. Xu, W. Zhang, Y. Yang, C.-X. Wang, and J. Thompson, “Wireless fractal cellular networks,” *IEEE Wireless Commun. Mag.*, vol. 23, no. 5, pp. 110–119, Oct. 2016.

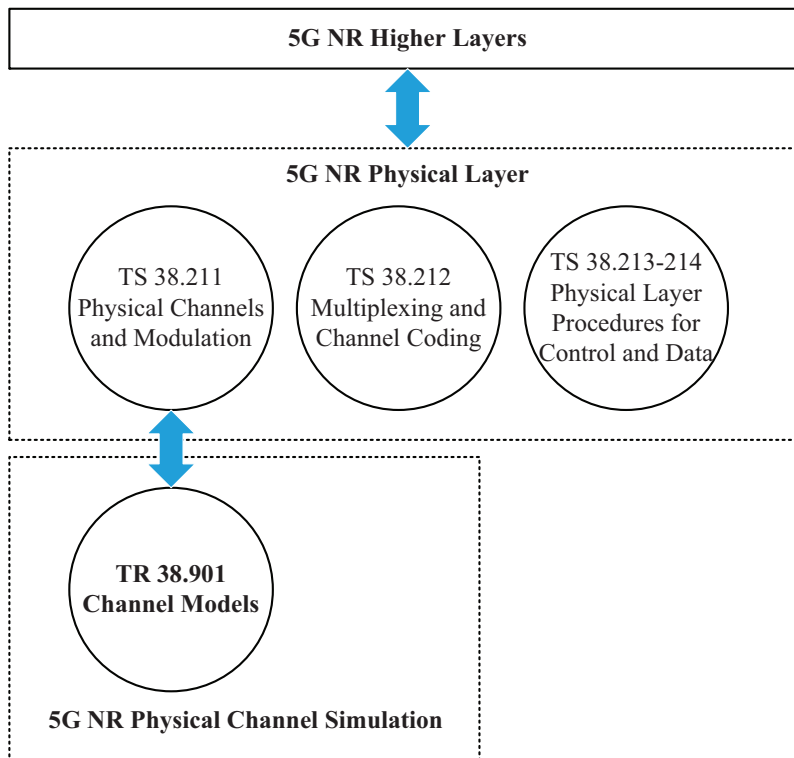


Fig. 1 Physical channel model and other layers in the 5G system

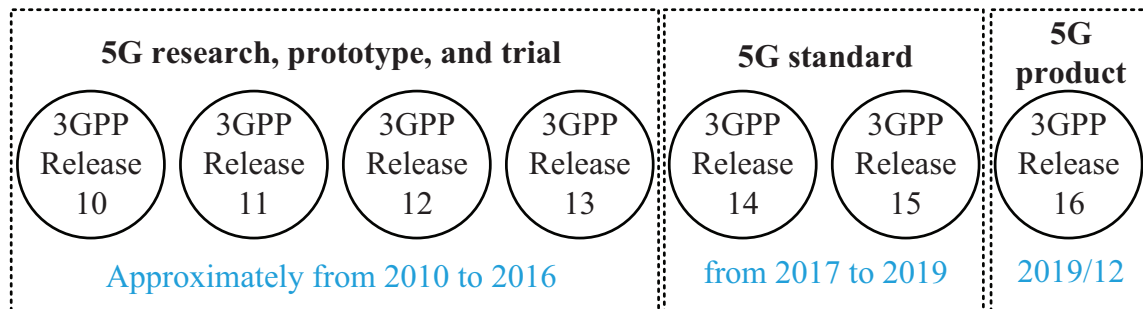


Fig. 2 3GPP standardization timeline

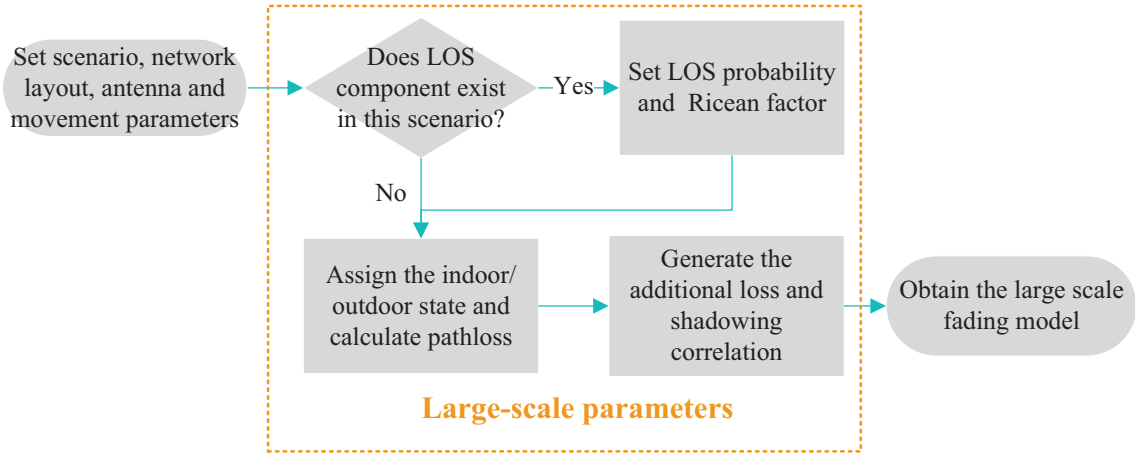


Fig. 3 Procedure of generating the large-scale fading

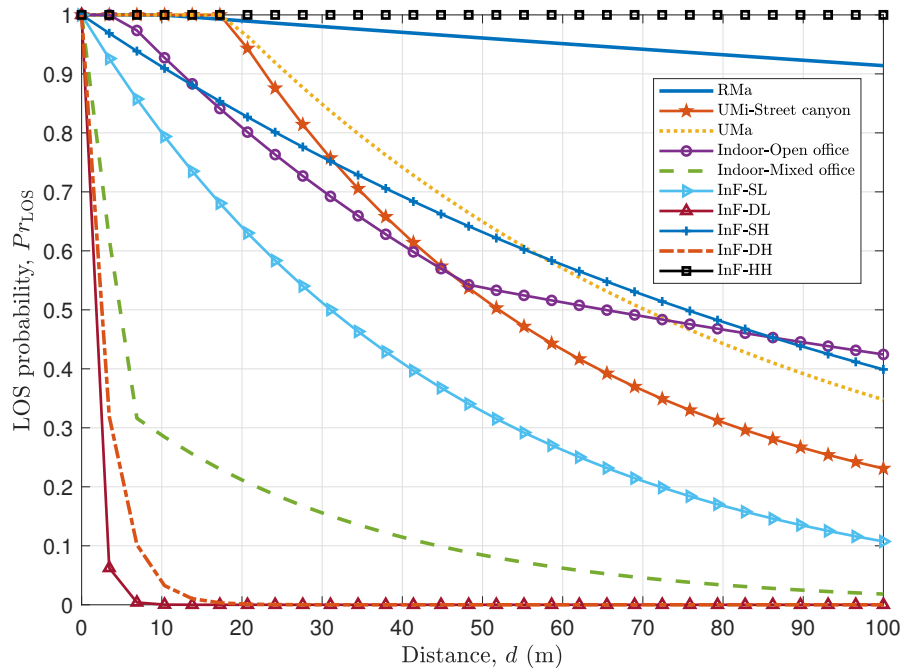


Fig. 4 LOS probabilities with different distances under different scenarios

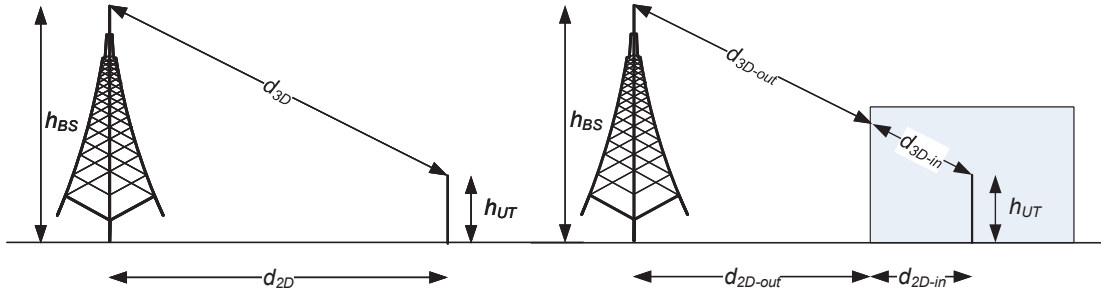


Fig. 5 Distance parameters of outdoor and indoor UTs

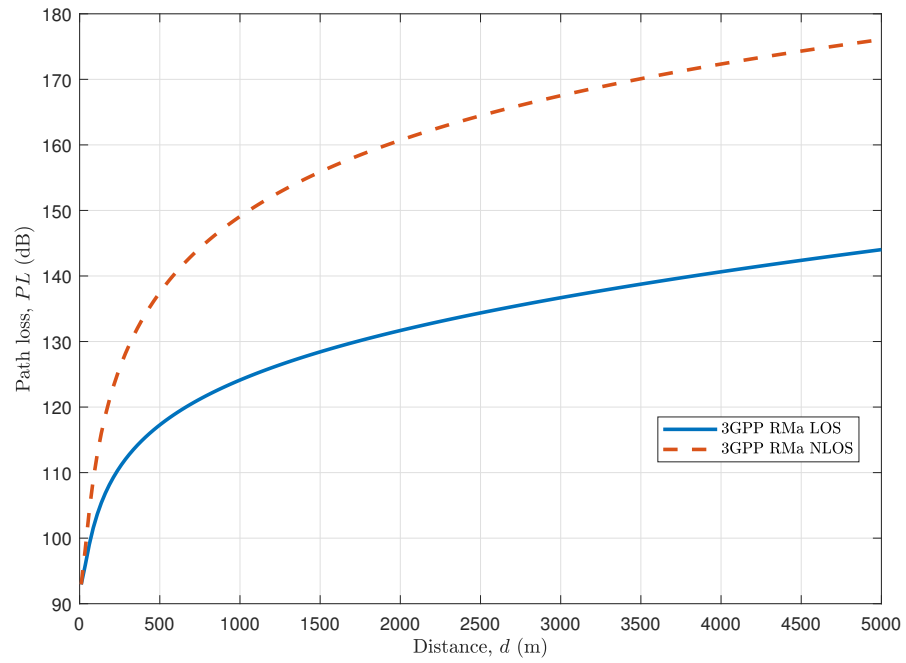


Fig. 6 Path loss in the RMa scenario

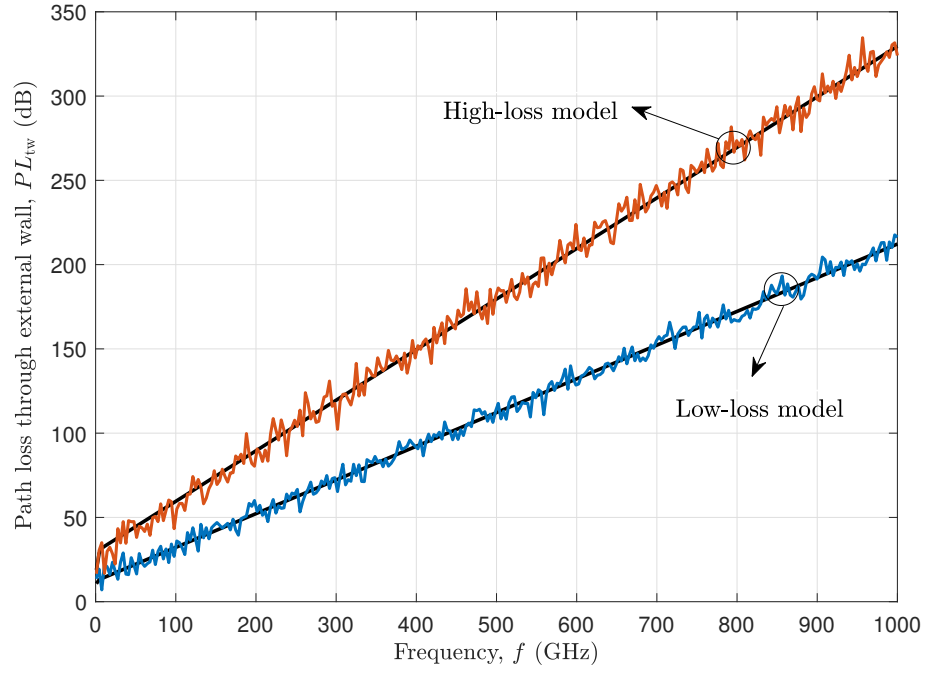


Fig. 7 Penetration losses of high-loss model and low-loss model

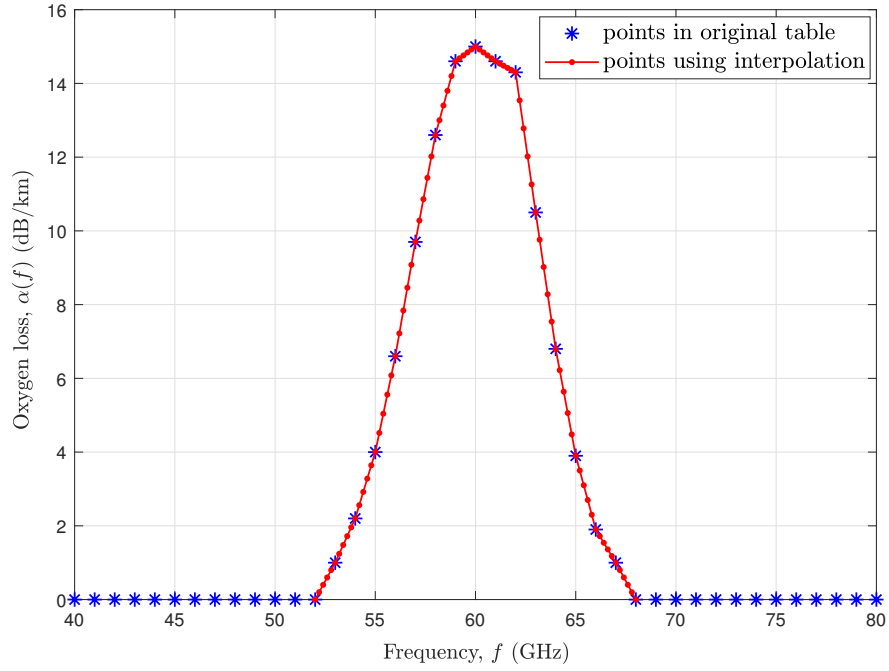


Fig. 8 Frequency dependent oxygen loss coefficient

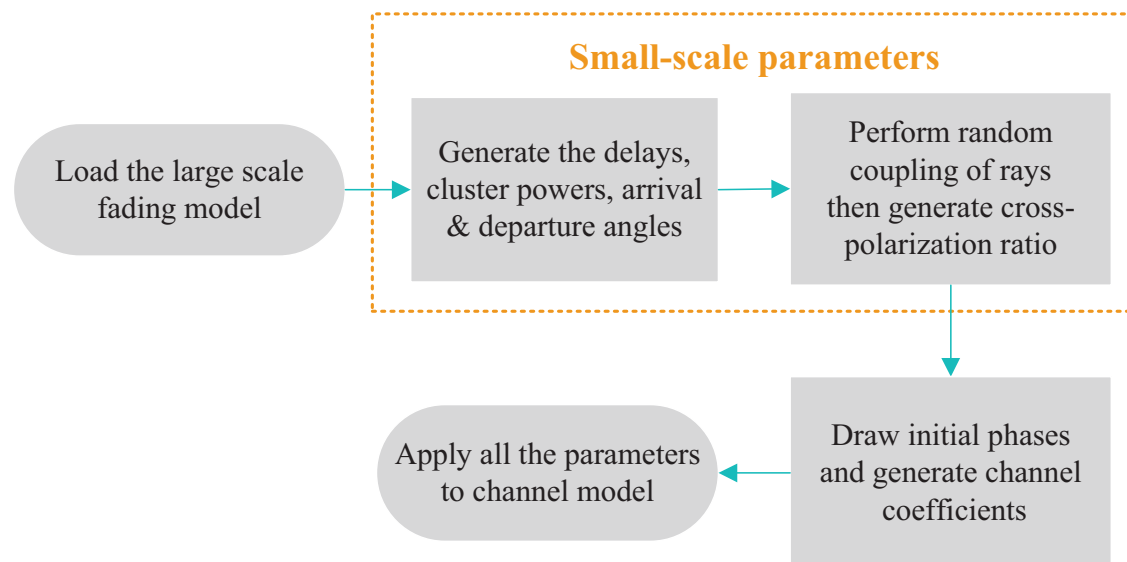
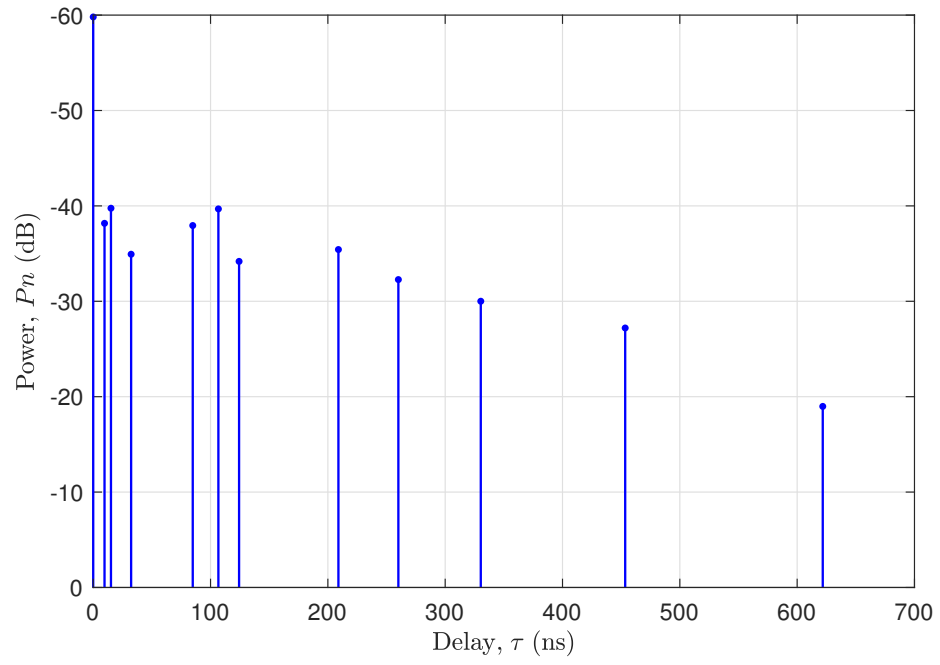
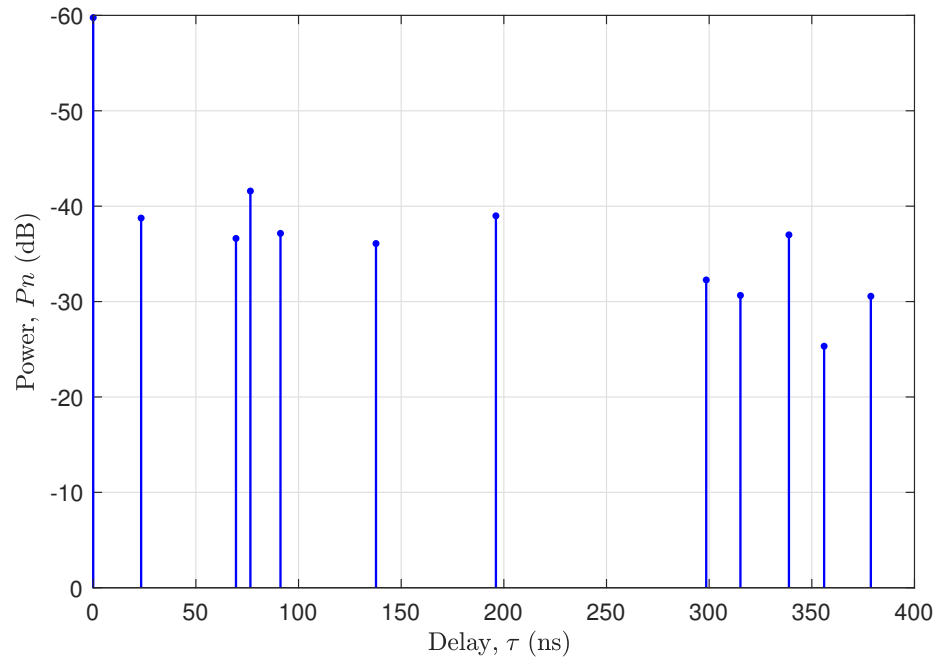


Fig. 9 Procedure of generating small-scale fading



(a) sample 1



(b) sample 2

Fig. 10 Two samples of PDP under the LOS scenario

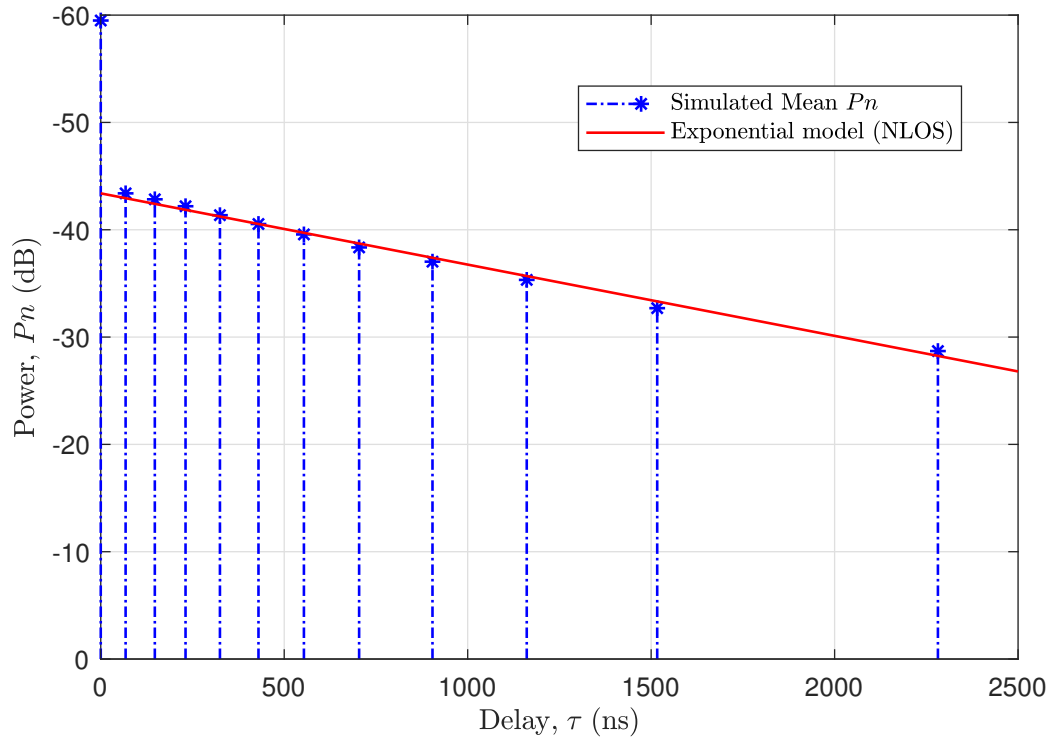


Fig. 11 Averaged PDP under the LOS scenario

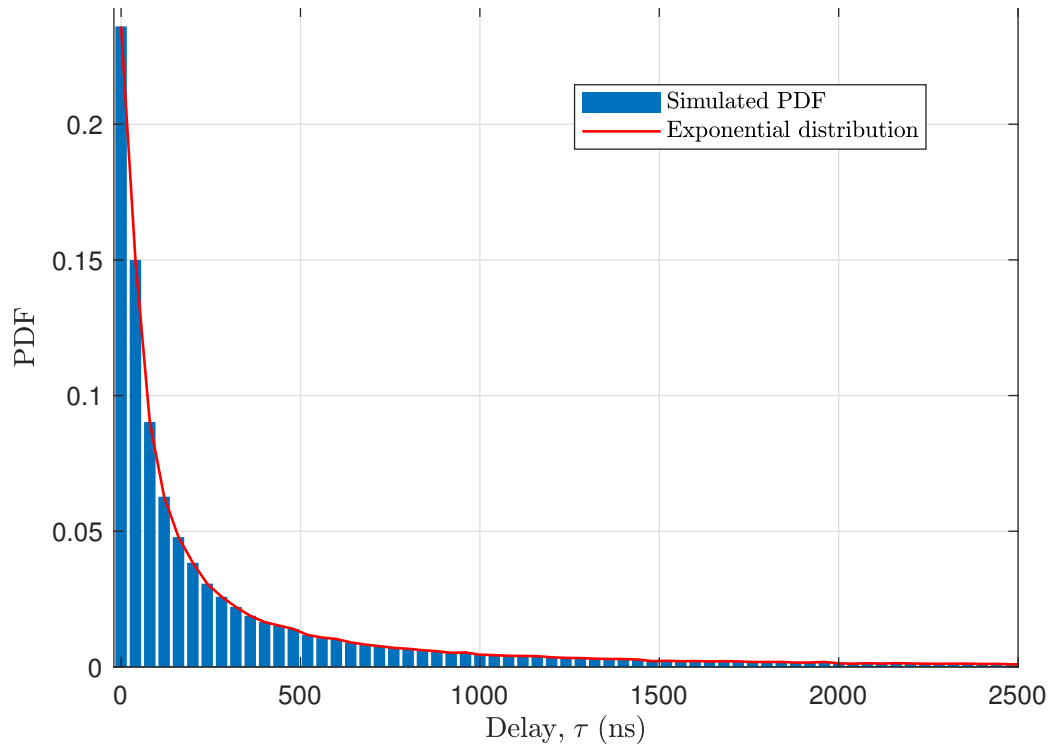
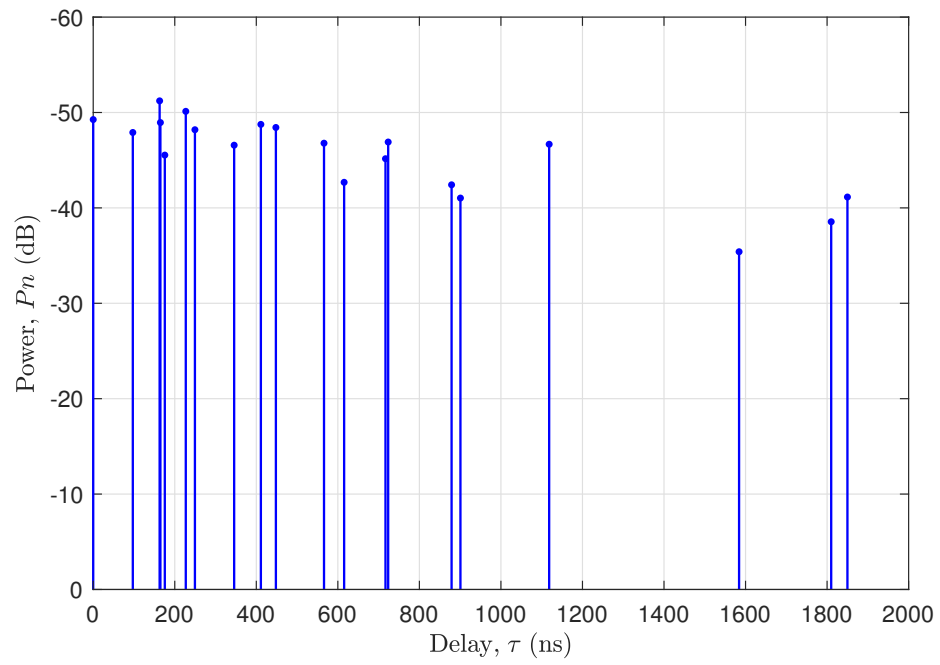
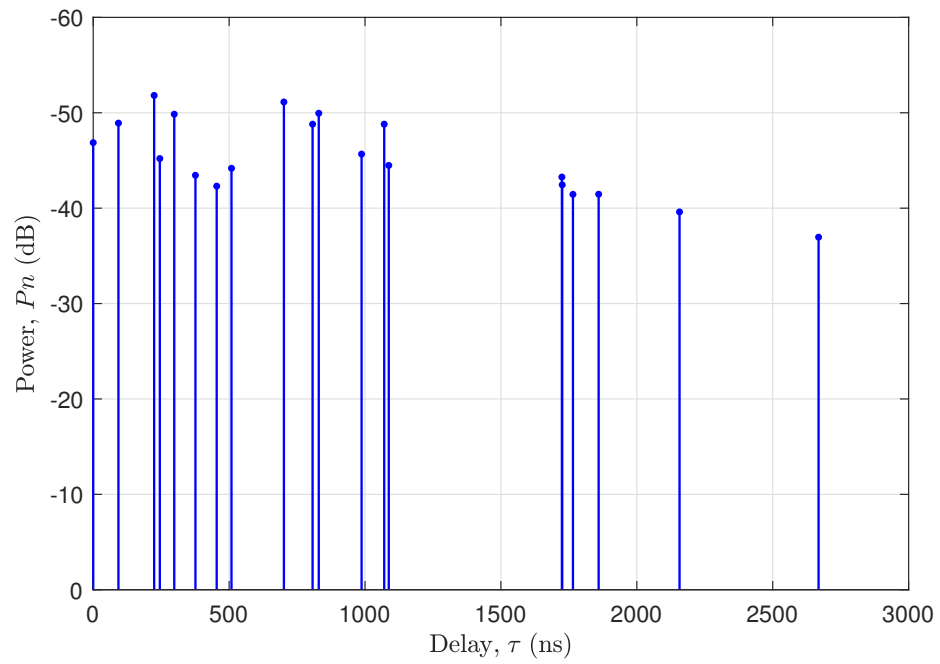


Fig. 12 Delay PDF under the LOS scenario





(a) sample 1



(b) sample 2

Fig. 13 Two samples of PDP under the NLOS scenario

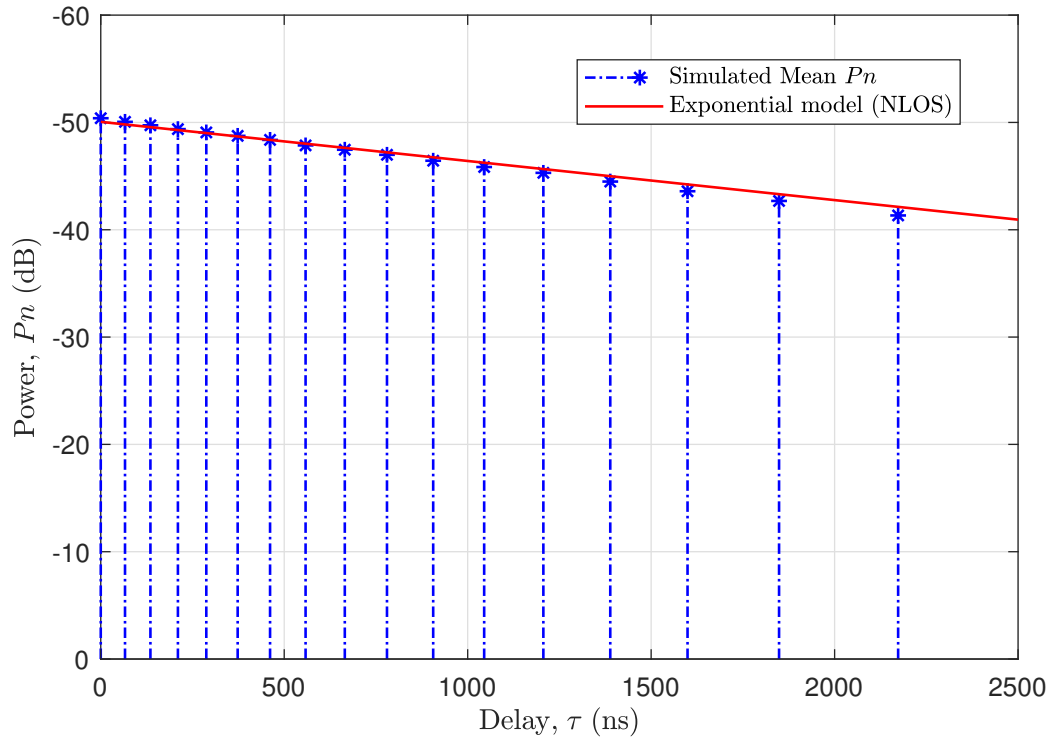


Fig. 14 Averaged PDP under the NLOS scenario

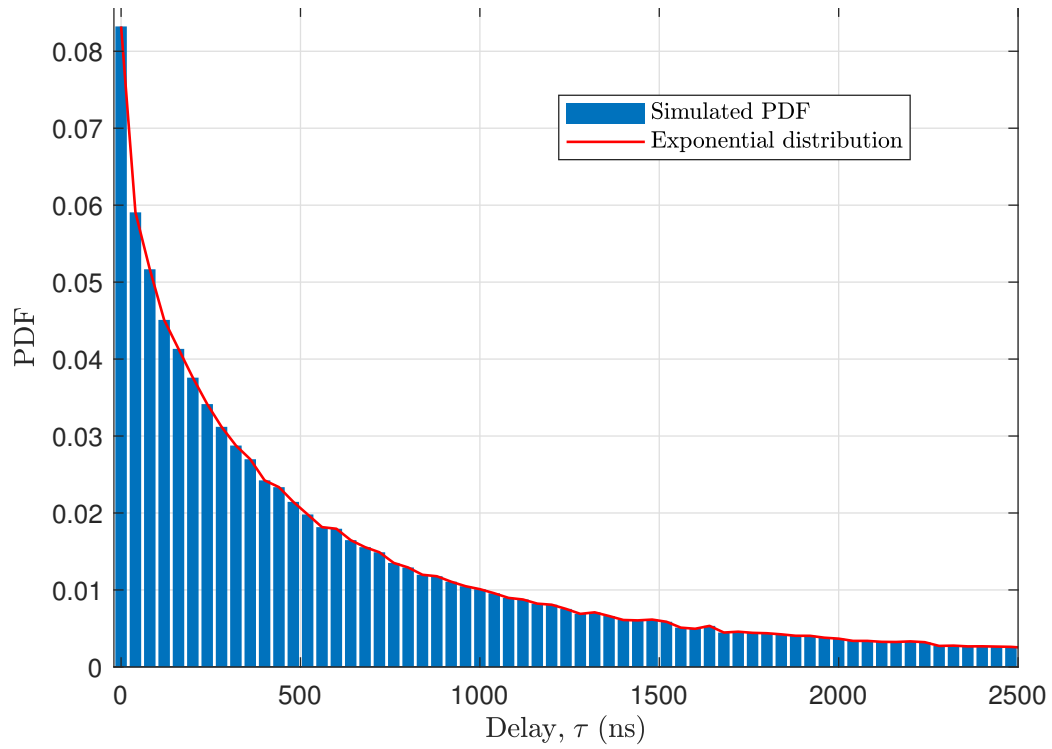


Fig. 15 Delay PDF under the NLOS scenario

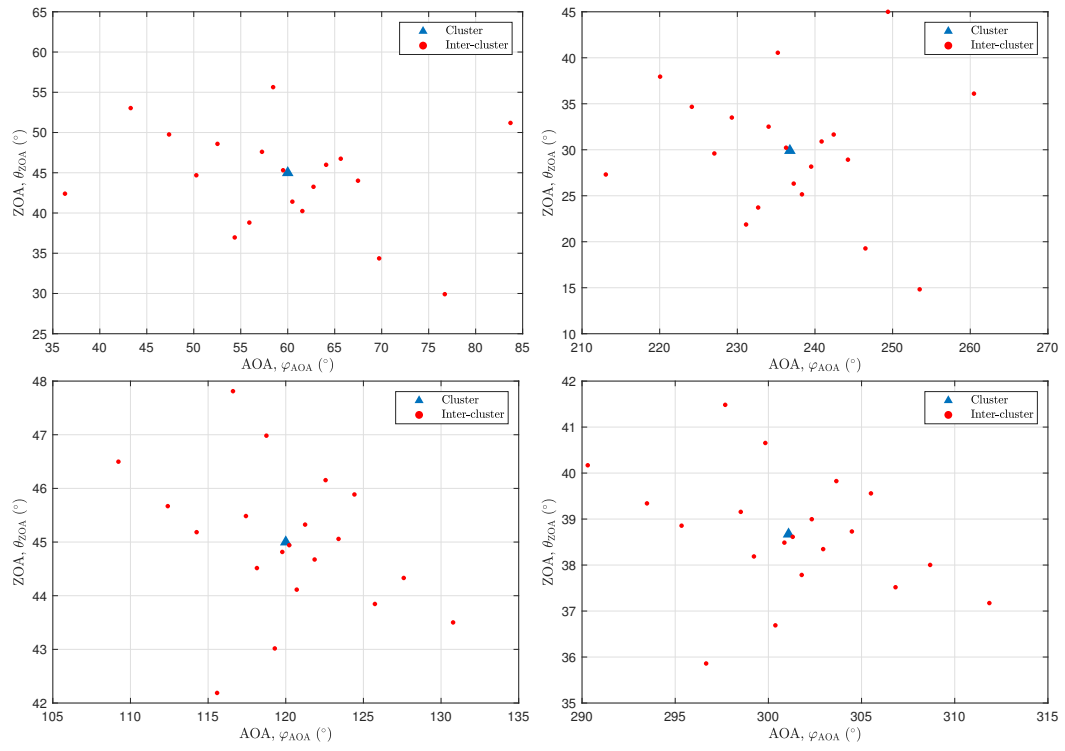


Fig. 16 Angular distributions of four different clusters

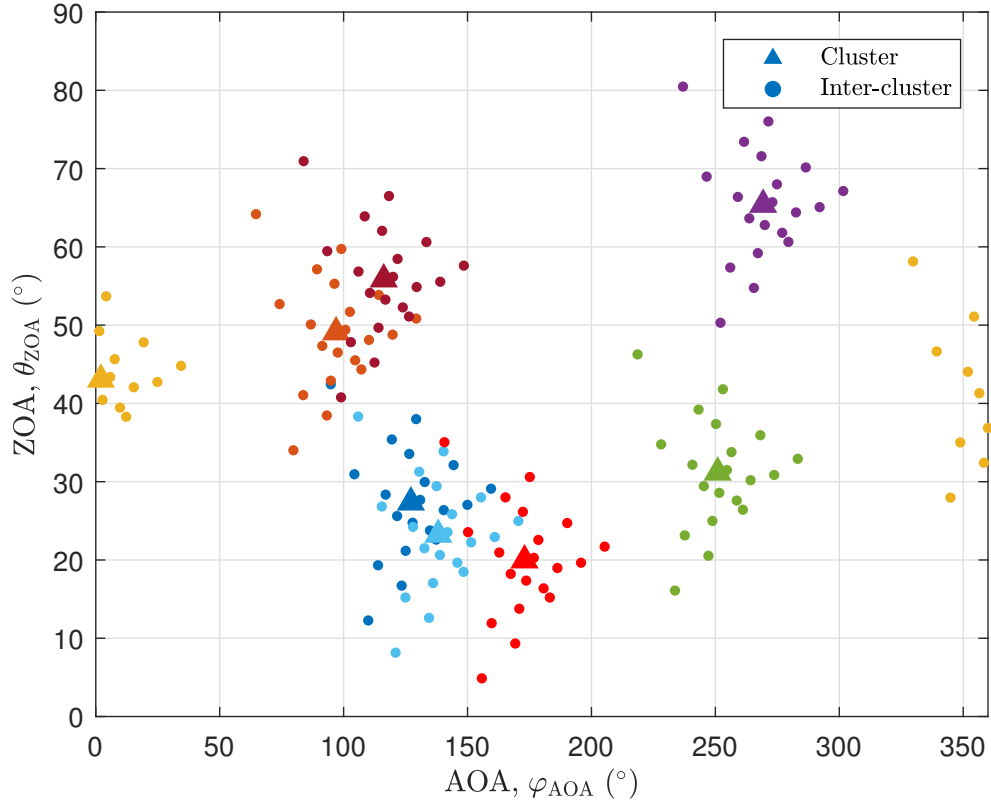


Fig. 17 Generated angles under a eight-cluster scenario

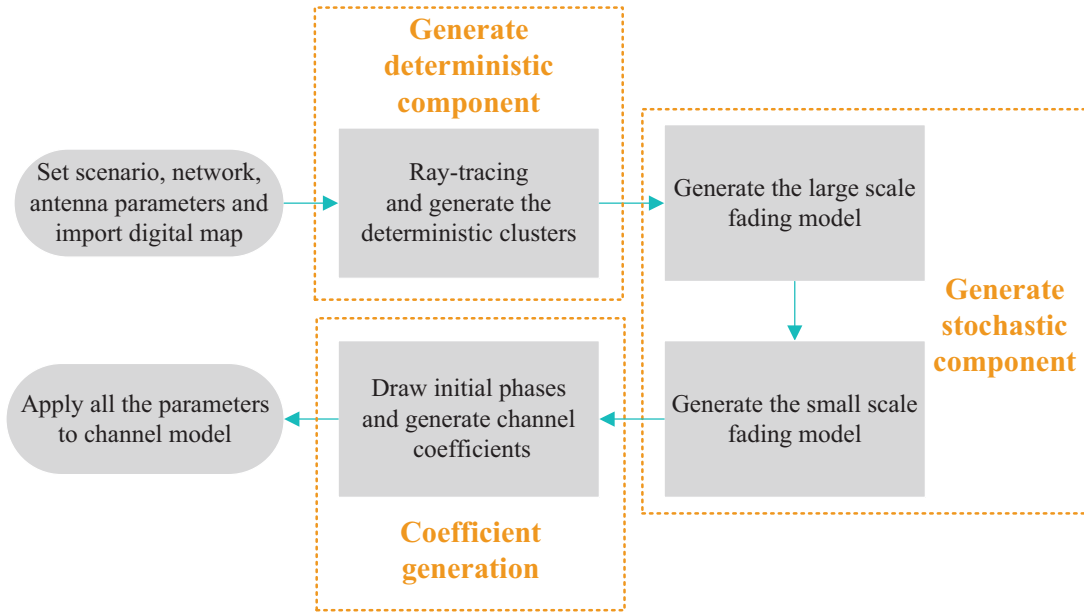
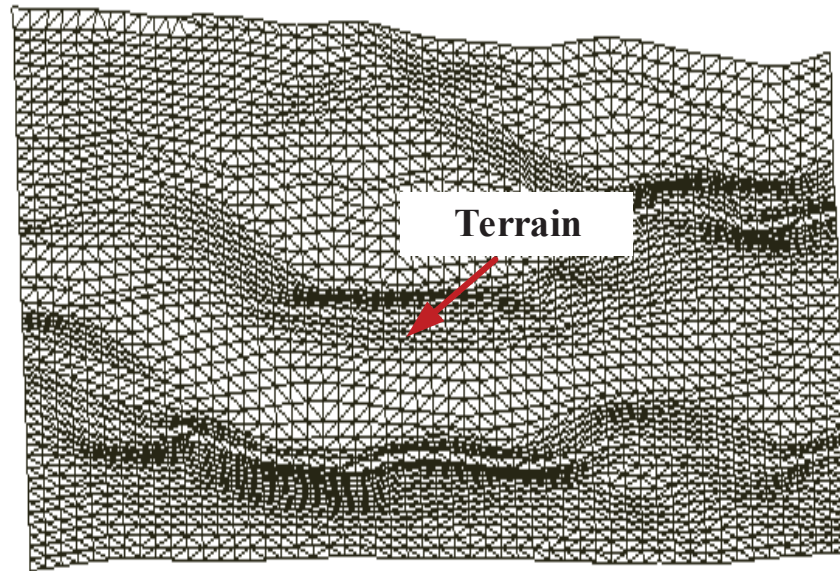
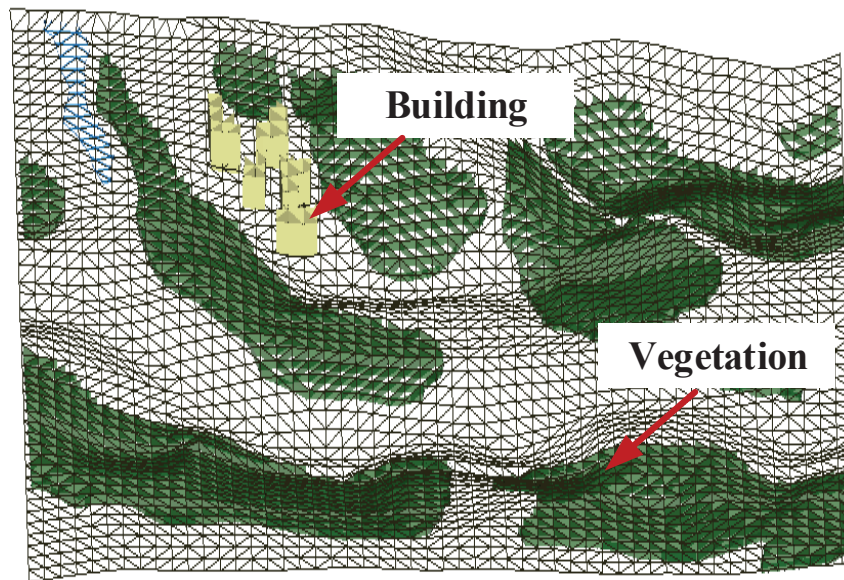


Fig. 18 Procedure of generating the map-based channel model



(a) Terrain



(b) Buildings and vegetation

Fig. 19 Reconstructed terrain, buildings and vegetation [75]

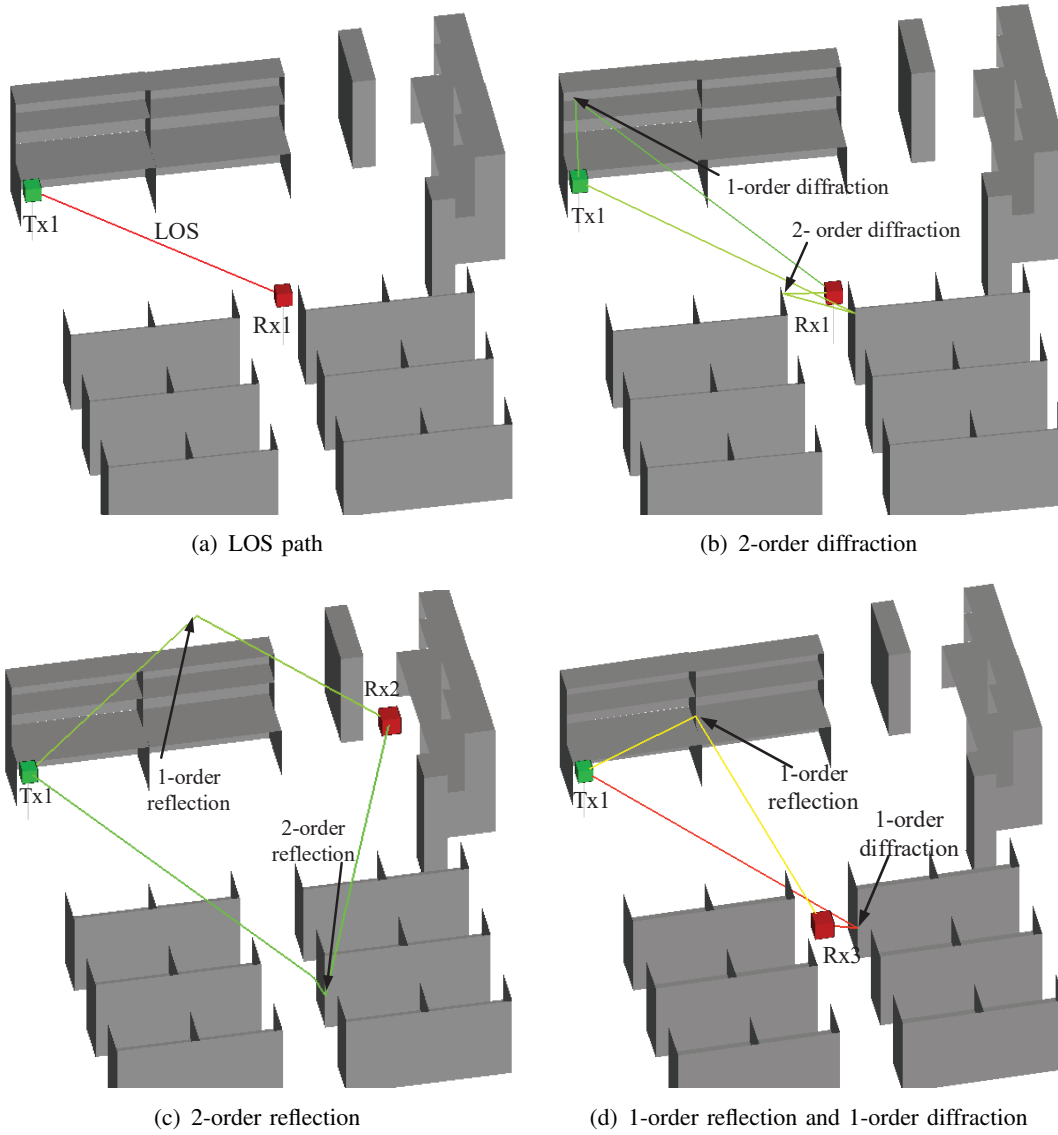


Fig. 20 Four different propagation mechanism

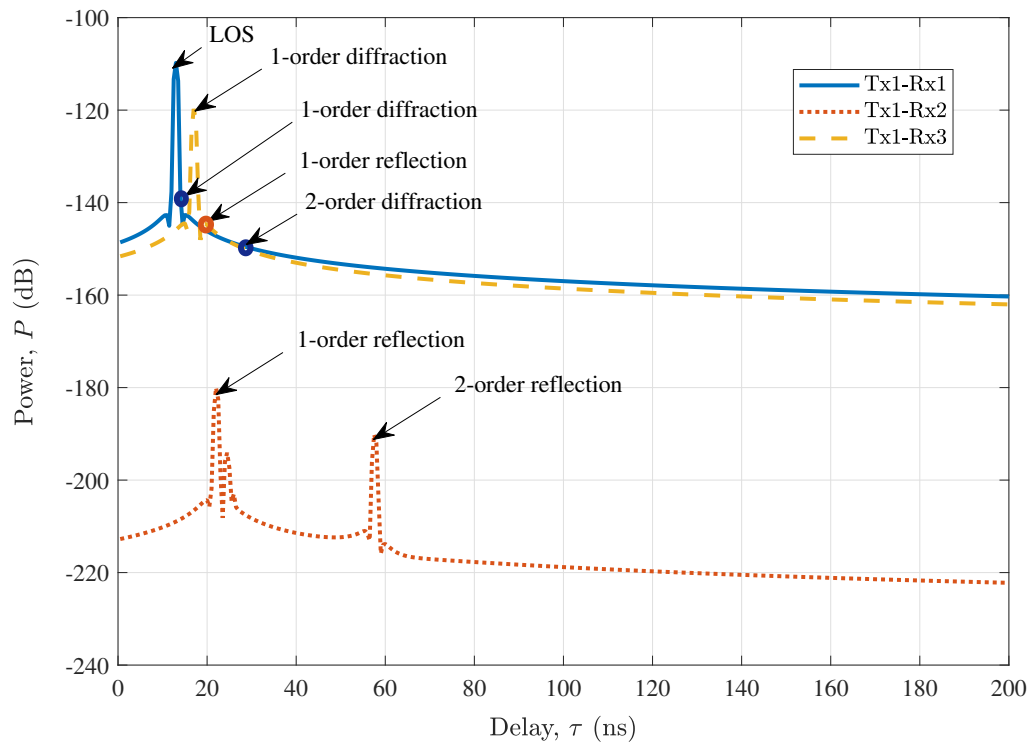


Fig. 21 Simulated PDPs by the RT method

Table I  
LOS probability models for different scenarios [34]

Scene	LOS probability
RMa	$Pr_{\text{LOS}} = \begin{cases} 1 & , d_{2\text{D-out}} \leq 10 \text{ m} \\ \exp\left(-\frac{d_{2\text{D-out}}-10}{1000}\right) & , 10 \text{ m} < d_{2\text{D-out}} \end{cases}$
UMi-Street canyon	$Pr_{\text{LOS}} = \begin{cases} 1 & , d_{2\text{D-out}} \leq 18 \text{ m} \\ \frac{18}{d_{2\text{D-out}}} + \exp\left(-\frac{d_{2\text{D-out}}}{36}\right) \left(1 - \frac{18}{d_{2\text{D-out}}}\right) & , 18 \text{ m} < d_{2\text{D-out}} \end{cases}$
UMa	$Pr_{\text{LOS}} = \begin{cases} 1 & , d_{2\text{D-out}} \leq 18 \text{ m} \\ \left[ \frac{18}{d_{2\text{D-out}}} + \exp\left(-\frac{d_{2\text{D-out}}}{63}\right) \left(1 - \frac{18}{d_{2\text{D-out}}}\right) \right] & , 18 \text{ m} < d_{2\text{D-out}} \\ \left[ 1 + C'(h_{\text{UT}})^{\frac{5}{4}} \left(\frac{d_{2\text{D-out}}}{100}\right)^3 \exp\left(-\frac{d_{2\text{D-out}}}{150}\right) \right] & \end{cases}$ where $C'(h_{\text{UT}}) = \begin{cases} 0 & , h_{\text{UT}} \leq 13 \text{ m} \\ \left(\frac{h_{\text{UT}}-13}{10}\right)^{1.5} & , 13 \text{ m} < h_{\text{UT}} \leq 23 \text{ m} \end{cases}$
Indoor-Mixed office	$Pr_{\text{LOS}} = \begin{cases} 1 & , d_{2\text{D-in}} \leq 1.2 \text{ m} \\ \exp\left(-\frac{d_{2\text{D-in}}-1.2}{4.7}\right) & , 1.2 \text{ m} < d_{2\text{D-in}} < 6.5 \text{ m} \\ 0.32 \exp\left(-\frac{d_{2\text{D-in}}-6.5}{32.6}\right) & , 6.5 \text{ m} \leq d_{2\text{D-in}} \end{cases}$
Indoor-Open office	$Pr_{\text{LOS}} = \begin{cases} 1 & , d_{2\text{D-in}} \leq 5 \text{ m} \\ \exp\left(-\frac{d_{2\text{D-in}}-5}{70.8}\right) & , 5 \text{ m} < d_{2\text{D-in}} \leq 49 \text{ m} \\ \exp\left(-\frac{d_{2\text{D-in}}-49}{211.7}\right) \cdot 0.54 & , 49 \text{ m} < d_{2\text{D-in}} \end{cases}$
InF-SL InF-SH InF-DL InF-DH	$Pr_{\text{LOS,subsc}}(d_{2\text{D}}) = \exp\left(-\frac{d_{2\text{D}}}{k_{\text{subsc}}}\right)$ where $k_{\text{subsc}} = \begin{cases} -\frac{d_{\text{clutter}}}{\ln(1-r)} & \text{for InF-SL and InF-DL} \\ -\frac{d_{\text{clutter}}}{\ln(1-r)} \cdot \frac{h_{\text{BS}}-h_{\text{UT}}}{h_c-h_{\text{UT}}} & \text{for InF-SH and InF-DH} \end{cases}$
InF-HH	$Pr_{\text{LOS}} = 1$
Note	$d_{\text{clutter}}$ is typical clutter size, $r$ is clutter density, $h_c$ is effective clutter height.



Table II  
Path loss and shadow fading STD for different scenarios [34]

Scenario	LOS/NLOS	Pathloss [dB]	Shadow fading STD [dB]	Applicability range, antenna height and default values
RMa	LOS	$PL_{\text{RMa-LOS}} = \begin{cases} PL_1 & 10 \text{ m} \leq d_{2D} \leq d_{\text{BP}} \\ PL_2 & d_{\text{BP}} \leq d_{2D} \leq 10 \text{ km} \end{cases}$ $PL_1 = 20\log_{10}(40\pi d_{3D}f_c/3) + \min(0.03h^{1.72}, 10)\log_{10}(d_{3D})$ $- \min(0.044h^{1.72}, 14.77) + 0.002\log_{10}(h)d_{3D}$ $PL_2 = PL_1(d_{\text{BP}}) + 40\log_{10}(d_{3D}/d_{\text{BP}})$	$\sigma_{\text{SF}}^{PL_1} = 4$  $\sigma_{\text{SF}}^{PL_2} = 6$	$5 \text{ m} \leq h \leq 50 \text{ m}$ $5 \text{ m} \leq W \leq 50 \text{ m}$ $10 \text{ m} \leq h_{\text{BS}} \leq 150 \text{ m}$ $1 \text{ m} \leq h_{\text{UT}} \leq 10 \text{ m}$
	NLOS	$PL_{\text{RMa-NLOS}} = \max(PL_{\text{RMa-LOS}}, PL'_{\text{RMa-NLOS}})$ for $10 \text{ m} \leq d_{2D} \leq 5 \text{ km}$ $PL'_{\text{RMa-NLOS}} = 161.04 - 7.1\log_{10}(W) + 7.5\log_{10}(h) -$ $(24.37 - 3.7(h/h_{\text{BS}})^2)\log_{10}(h_{\text{BS}}) + (43.42 - 3.1\log_{10}(h_{\text{BS}}))(\log_{10}(d_{3D}) - 3)$ $- (3.2(\log_{10}(11.75h_{\text{UT}}))^2 - 4.97) + 20\log_{10}(f_c)$	$\sigma_{\text{SF}} = 8$	
UMa	LOS	$PL_{\text{UMa-LOS}} = \begin{cases} PL_1 & 10 \text{ m} \leq d_{2D} \leq d'_{\text{BP}} \\ PL_2 & d'_{\text{BP}} \leq d_{2D} \leq 5 \text{ km} \end{cases}$ $PL_1 = 28.0 + 22\log_{10}(d_{3D}) + 20\log_{10}(f_c)$ $PL_2 = 28.0 + 40\log_{10}(d_{3D}) + 20\log_{10}(f_c) - 9\log_{10}((d'_{\text{BP}})^2 + (h_{\text{BS}} - h_{\text{UT}})^2)$	$\sigma_{\text{SF}} = 4$	$1.5 \text{ m} \leq h_{\text{UT}} \leq 22.5 \text{ m}$ $h_{\text{BS}} = 25 \text{ m}$
	NLOS	$PL_{\text{UMa-NLOS}} = \max(PL_{\text{UMa-LOS}}, PL'_{\text{UMa-NLOS}})$ for $10 \text{ m} \leq d_{2D} \leq 5 \text{ km}$ $PL'_{\text{UMa-NLOS}} = 13.54 + 39.08\log_{10}(d_{3D}) + 20\log_{10}(f_c) - 0.6(h_{\text{UT}} - 1.5)$	$\sigma_{\text{SF}} = 6$	
UMi - Street Canyon	LOS	$PL_{\text{UMi-LOS}} = \begin{cases} PL_1 & 10 \text{ m} \leq d_{2D} \leq d'_{\text{BP}} \\ PL_2 & d'_{\text{BP}} \leq d_{2D} \leq 5 \text{ km} \end{cases}$ $PL_1 = 32.4 + 21\log_{10}(d_{3D}) + 20\log_{10}(f_c)$ $PL_2 = 32.4 + 40\log_{10}(d_{3D}) + 20\log_{10}(f_c) - 9.5\log_{10}((d'_{\text{BP}})^2 + (h_{\text{BS}} - h_{\text{UT}})^2)$	$\sigma_{\text{SF}} = 4$	$1.5 \text{ m} \leq h_{\text{UT}} \leq 22.5 \text{ m}$ $h_{\text{BS}} = 10 \text{ m}$
	NLOS	$PL_{\text{UMi-NLOS}} = \max(PL_{\text{UMi-LOS}}, PL'_{\text{UMi-NLOS}})$ for $10 \text{ m} \leq d_{2D} \leq 5 \text{ km}$ $PL'_{\text{UMi-NLOS}} = 35.3\log_{10}(d_{3D}) + 22.4 + 21.3\log_{10}(f_c) - 0.3(h_{\text{UT}} - 1.5)$	$\sigma_{\text{SF}} = 7.82$	
InH - Office	LOS	$PL_{\text{InH-LOS}} = 32.4 + 17.3\log_{10}(d_{3D}) + 20\log_{10}(f_c)$	$\sigma_{\text{SF}} = 3$	$1 \text{ m} \leq d_{3D} \leq 150 \text{ m}$
	NLOS	$PL_{\text{InH-NLOS}} = \max(PL_{\text{InH-LOS}}, PL'_{\text{InH-NLOS}})$ $PL'_{\text{InH-NLOS}} = 38.3\log_{10}(d_{3D}) + 17.30 + 24.9\log_{10}(f_c)$	$\sigma_{\text{SF}} = 8.03$	
InF	LOS	$PL_{\text{LOS}} = 31.84 + 21.50\log_{10}(d_{3D}) + 19.00\log_{10}(f_c)$	$\sigma_{\text{SF}} = 4$	$1 \text{ m} \leq d_{3D} \leq 600 \text{ m}$
	NLOS	$\text{InF-SL: } PL = 33 + 25.5\log_{10}(d_{3D}) + 20\log_{10}(f_c)$ $PL_{\text{NLOS}} = \max(PL, PL_{\text{LOS}})$	$\sigma_{\text{SF}} = 5.7$	
		$\text{InF-DL: } PL = 18.6 + 35.7\log_{10}(d_{3D}) + 20\log_{10}(f_c)$ $PL_{\text{NLOS}} = \max(PL, PL_{\text{LOS}}, PL_{\text{InF-SL}})$	$\sigma_{\text{SF}} = 7.2$	
		$\text{InF-SH: } PL = 32.4 + 23.0\log_{10}(d_{3D}) + 20\log_{10}(f_c)$ $PL_{\text{NLOS}} = \max(PL, PL_{\text{LOS}})$	$\sigma_{\text{SF}} = 5.9$	
		$\text{InF-DH: } PL = 33.63 + 21.9\log_{10}(d_{3D}) + 20\log_{10}(f_c)$ $PL_{\text{NLOS}} = \max(PL, PL_{\text{LOS}})$	$\sigma_{\text{SF}} = 4$	
Notes:	1. $f_c$ is in GHz and $d$ is in meter. 2. $h$ is average building height and $W$ is average street width.			

Table III  
Material penetration loss [34]

Material	Penetration loss [dB]
Standard multi-pane glass	$L_{\text{glass}} = 2 + 0.2f$
Infrared reflecting (IRR) glass	$L_{\text{IRRglass}} = 23 + 0.3f$
Concrete	$L_{\text{concrete}} = 5 + 4f$
Wood	$L_{\text{wood}} = 4.85 + 0.12f$

Table IV  
Two empirical path loss models [34]

Model type	Path loss through external wall [dB]	STD [dB]
Low-loss model	$5 - 10 \log_{10} \left( 0.3 \cdot 10^{\frac{-L_{\text{glass}}}{10}} + 0.7 \cdot 10^{\frac{-L_{\text{concrete}}}{10}} \right)$	4.4
High-loss model	$5 - 10 \log_{10} \left( 0.7 \cdot 10^{\frac{-L_{\text{IRRglass}}}{10}} + 0.3 \cdot 10^{\frac{-L_{\text{concrete}}}{10}} \right)$	6.5

Table V  
Oxygen loss coefficient [34]

$f$ [GHz]	0–52	53	54	55	56	57	58	59	60	61	62	63	64	65	66	67	68–100
$\alpha(f)$ [dB/km]	0	1	2.2	4	6.6	9.7	12.6	14.6	15	14.6	14.3	10.5	6.8	3.9	1.9	1	0

Table VI  
Parameters in the simulation of delay and power [34]

Scenario		UMa	
		LOS	NLOS
Delay spread $DS$ $\lg DS = \log_{10}(DS/1s)$	$\mu_{\lg DS}$	$-6.955 - 0.0963\log_{10}(f_c)$	$-6.28 - 0.204\log_{10}(f_c)$
	$\sigma_K$	0.66	0.39
K-factor $K$ [dB]	$\mu_K$	9	N/A
	$\sigma_K$	3.5	N/A
Delay scaling parameter $r_\tau$		2.5	2.3
Number of clusters $N$		12	20
Scaling constant $C_\tau$		$0.7705 - 0.0433K +$ $0.0002K^2 + 0.000017K^3$	N/A
Per cluster shadowing STD $\zeta$ [dB]		3	3
Frequency $f_c$ [GHz]		6	6

Table VII  
Ray offset angles within a cluster, given for rms angle spread normalized to 1 [34]

Ray number $m$	Basis vector of offset angles $\alpha_m$
1,2	$\pm 0.0447$
3,4	$\pm 0.1413$
5,6	$\pm 0.2492$
7,8	$\pm 0.3715$
9,10	$\pm 0.5129$
11,12	$\pm 0.6797$
13,14	$\pm 0.8844$
15,16	$\pm 1.1481$
17,18	$\pm 1.5195$
19,20	$\pm 2.1551$

Table VIII  
Parameters in the simulation of AOA and ZOA [34]

Scenario		UMa	
		LOS	NLOS
AOA spread $ASA$ $\lg ASA = \log_{10}(ASA/1^\circ)$	$\mu_{\lg ASA}$	1.81	$2.08 - 0.27\log_{10}(f_c)$
	$\sigma_{\lg ASA}$	0.20	0.11
ZOA spread $ZSA$ $\lg ZSA = \log_{10}(ZSA/1^\circ)$	$\mu_{\lg ZSA}$	0.95	$-0.3236\log_{10}(f_c) + 1.512$
	$\sigma_{\lg ZSA}$	0.16	0.16
K-factor $K$ [dB] <small>View publication stats</small>	$\mu_K$	9	N/A
	$\sigma_K$	3.5	N/A
Number of rays per cluster $M$		20	20
Scaling factor $C_\varphi$		$1.289 \cdot (1.1035 + 0.028K - 0.002K^2 + 0.0001K^3)$	1.289
Scaling factor $C_\theta$		$1.178 \cdot (1.3086 + 0.0339K - 0.0077K^2 + 0.0002K^3)$	1.178
Cluster ASA $c_{ASA}$ [deg]		11	15
Cluster ZSA $c_{ZSA}$ [deg]		7	7
Frequency $f_c$ [Ghz]		6	6